X-ray photoemission studies of bimetallic Pt-Ga, Pd-Ga and Rh-Ga catalysts

Untersuchungen an bimetallischen Pt-Ga, Pd-Ga und Rh-Ga Katalysatoren mittels Röntgenphotoelektronenspektroskopie

Der Naturwissenschaftlichen Fakultät der
Friedrich-Alexander Universtität Erlangen-Nürnberg
zur Erlangung des Doktorgrades Dr. rer. nat.

vorgelegt von

Mathias F. Grabau
aus Nürnberg

Als Dissertation genehmigt von der Naturwissenschaftlichen Fakultät der Friedrich-Alexander-Universität Erlangen-Nürnberg

Tag der mündlichen Prüfung:	10.12.2018
Vorsitzender des Promotionsorgans:	Prof. Dr. Georg Kreimer
Gutachter:	Prof. Dr. Hans-Peter Steinrück
	Prof. Dr. Jörg Libuda

Contents

1. Introduction

1.1. General aspects of catalysis

The term catalysis was first used by Berzelius in 1835 [1, 2] to describe the ability of certain substances to enhance a chemical reaction without being consumed in-, or being changed by it. Ostwald, awarded with the Nobel Prize in Chemistry in 1909 for his work [3], shaped the understanding of the concept of catalysis at that time into his well known quote [2, 4] almost a century later.

"Ein Katalysator ist jeder Stoff, der ohne im Endprodukt einer chemischen Reaktion zu erscheinen, ihre Geschwindigkeit verändert."

Sabatier extended this concept including intermediates that have suitable stability to not produce a thermodynamic sink, but allow for activation of the reactant, and formation of the product.[1] Within the following century the importance and diversity of catalysis steadily increased, and adapted to the increasing demand for food and resources. The paradigms formulated by Berzelius, Ostwald and Sabatier, however, still are accepted to hold today. Among the most important catalyzed reactions to mention are the different flavors of cracking and reforming reactions, as well as processes like Haber-Bosch, and ammonia oxidation that provide a base feedstock for the production of fertilizers, fuels and fine chemicals. Estimates state that >35 % of the worlds gross domestic product, and 80 % of all added value in chemical industry is based on catalysis. Heterogeneous catalysts are estimated to have a market share of 85 %.[5]

A schematic representation of a catalysts influence on a reaction pathway is shown in Figure 1.1 (a). In Figure 1.1 (b) a schematic of the catalytic cycle leading to formation of product P from reactant R is shown. Reactants or products of the reaction are not changed by the addition of a catalyst. This implies that also thermodynamics, limiting equilibrium conversion, remain unchanged. However, by forming un- or metastable reaction intermediates with the catalyst, drawn in green, the highest occurring activation energy may be reduced. These intermediates are for example molecules coordinated to the catalyst complex in homogeneous solution or species formed by adsorption or reaction on the surface of a heterogeneous catalyst. As the highest activation barrier defines the so-called rate-determining step of a reaction pathway, according to transition state theory and chemical kinetics the overall reaction rate will be increased. This provides higher efficiency of the catalytic process in industrial application.

Also beneficial to the creation of value in chemical industry is an increase in selectivity, as less cost results from energy-demanding separation of the desired product P from side products. Thus any modification of the catalyst, which results in destabilization of intermediates leading to the

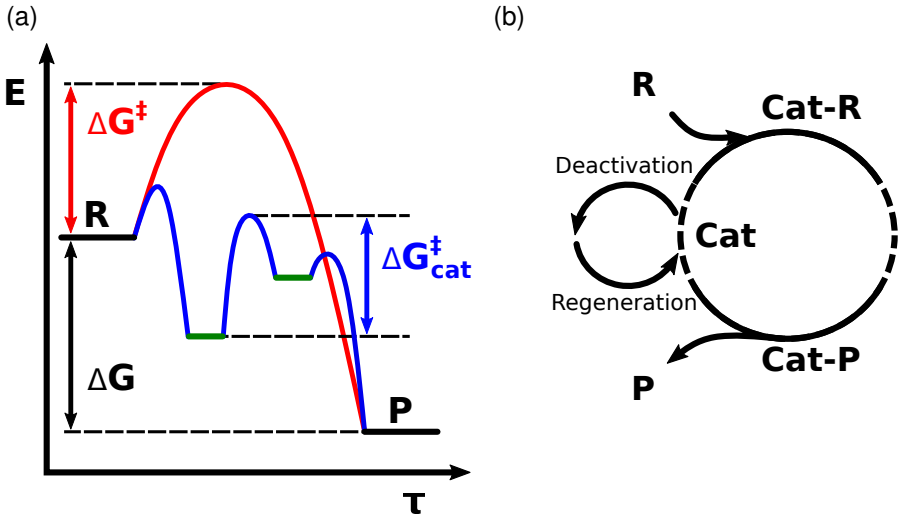

Figure 1.1.: (a) Schematic representations of uncatalyzed and catalyzed reaction in a Gibbs energy vs. reaction coordinate diagram. (b) Catalytic cycle; dashed parts indicate possible side-reactions, as well as processes leading to catalyst poisoning or deactivation.

formation of undesired side products and is therefore enabling the application of kinetic control towards the desired product is of great value. Further, long-term stability and fast and low-cost regeneration of the catalyst are vital to the economic aspects of a catalytic reaction. This implies that ideally the catalyst remains active during as many catalytic cycles as possible and that a catalyst, deactivated by poisoning in side reactions indicated as dashed line in Figure 1.1 (b) or by sintering, can be subjected to a treatment restoring its original activity and selectivity.

Activity, stability and selectivity can be influenced by the addition of suitable promoters, and the combination of different elements into an industrially applicable heterogeneous catalyst is in fact very common since the beginning of industrial catalysis. Examples range from the aforementioned ammonia synthesis ($Fe_2O_3/K_2O/Al_2O_3$) and -oxidation (Pt/Rh) to a variety of dopants (K, Ba, Fe, Mn) being used to promote the supported Ni catalyst used in steam reforming of light aliphatic hydrocarbons.[5–10] This additive-based improvement of catalysts, however, was and still is typically based strongly on empirical data and promising catalyst materials are often found by material screening. With increased computing powers and improved abilities to accurately produce and evaluate big data sets, such material screening is also done in an automated way typically referred to as high-throughput screening.[5, 11–13] Also theoretical chemistry, partly by combining quantum chemistry and methodology from process engineering, targets a multi-scale modeling and theory-based design of catalysts and catalytic reactions.[14–19]

1.2. Pressure and material gaps

The surface scientist's approach is the understanding and rationalization of synergistic effects arising from the combination of different materials into a well-functioning catalyst based on the

examination of model systems. The extrapolation of the so-gained knowledge into regimes of the parameter space common to industrial catalysis is desirable. However, this is often not possible because model systems per definition lack the complexity of real catalysts. Furthermore the elevated pressure of reactants induces effects like mass-transfer limitations or dynamic restructuring of the catalyst surface. It is therefore essential to bridge the so-called *pressure and material gaps*, depicted schematically in Figure 1.2, by providing experimental data collected from more complex models or real catalysts under temperature and pressure conditions similar to those present in a chemical reactor to enable a knowledge-driven optimization of catalysts.

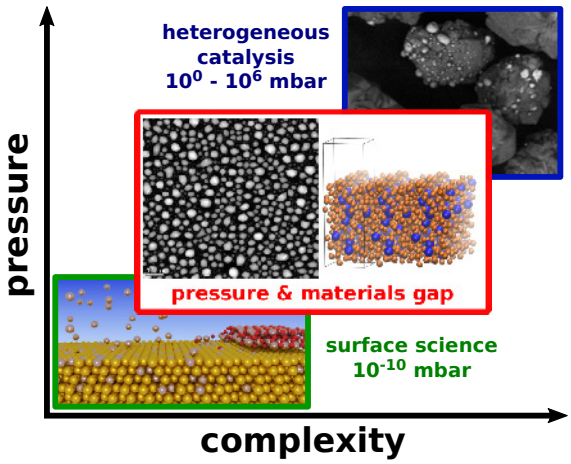

Figure 1.2.: Schematic representation of the pressure and material gaps.

In surface science, typically ultra-high vacuum conditions are necessary to ensure the cleanliness of surfaces that are to be examined during preparation and measurement. This allows for unambiguous interpretation of the collected data. Also, many of the used surface analysis techniques rely on high or ultra-high vacuum conditions to avoid complications like high-voltage flashover, contaminations or corrosion. In particular, methods for surface analysis that rely on ions or electrons as probe, due to the high probability of charged particles to interact with matter, suffer from elevated pressures as signal attenuation by the gas phase prolongs acquisition times. Ambient pressure spectroscopy and -microscopy is thus a challenging field for engineers, technicians and scientists. Despite these challenges, an increasing number of studies bridging the pressure and material gaps are published including entire journal issues devoted to the in-situ examination of (model) catalysts. [20–44]

In this thesis, an attempt to bridge the material gaps is made by the examination of oxide-supported bimetallic catalysts, or low-temperature-melting metallic alloys in liquid or biphasic state as a model system for the former. This is partly done by utilizing near-ambient pressure x-ray photoelectron spectroscopy (NAP-XPS), which enables to collect in-situ data under elevated pressures of up to 1 mbar

1.3. The Pd/Pt/Rh-Ga bimetallic catalysts in the dehydrogenation of light alkanes

The dehydrogenation of alkanes is a demanding reaction. Maximum conversion is limited by thermodynamic equilibrium; as the reaction is endothermic, high temperatures are needed to achieve reasonable yields. This, however, will not only shift the equilibrium towards the dehydrogenated product, but it will also facilitate unwanted, parasitic side-reactions including cracking and the formation of coke. The latter is responsible for the necessity of frequent catalyst regeneration by coke burn-off, which is typical for all the industrially applied dehydrogenation processes where regeneration time roughly equals the on-stream time. Reaction temperatures in these processes range from 770 to 970 K at pressures of 0.2 to 6 bar, resulting in approx. 50 % conversion for light alkanes at 90 % selectivity for the corresponding alkene. Catalysts used in the commercially operated plants are either Pt-Sn bimetallics supported on alumina (Oleflex, STAR) or mixed metal oxides CrO_x/alumina (CATOFIN, FBD). Catalyst lifetimes range from 1 to 3 years. All of the commercially operating processes additionally utilize alkaline promoters.[45–49] The thermodynamics of the reaction can be influenced for the benefit of conversion by adding sources of oxygen like molecular oxygen (air) or carbondioxide, or oxidizing reagents like halogens.[50–53] Clearly, novel catalysts or additives that enable a dehydrogenation process being run at higher selectivity or stability are of great value.

Scientific approaches to the catalytic dehydrogenation of alkanes, beside Pt-based bimetallics, include the use of different alumina-supported metal oxides such as CrO_x, VO_x, MoO_x, InO_x and GaO_x.[49] The Pt-based catalysts are found best-performing with specific activities ($\frac{\text{mole}_{\text{product}}}{\text{mole}_{\text{catalyst}} \cdot \text{time}}$) in the range of 1×10^{-2} to $2\,s^{-1}$, while metal oxide catalysts show only moderate activity in the range of 1×10^{-6} to $1 \times 10^{-3}\,s^{-1}$. The combination of Ga or Ga_2O_3 supports with Pt also has been demonstrated in multiple studies to provide promising catalyst candidates. It was shown that the addition of Pt to a alumina supported Ga_2O_3 catalyst (Pt content of 1.2 and 2.5 at.% with respect to Ga) significantly increases stability in combination with a moderate increase in activity. Furthermore, K promotion is demonstrated to drastically reduce coke deposition for both the pure Ga and the bimetallic catalyst.[54] Other studies demonstrate the formation of different Pt-Ga alloy phases upon high temperature (>780 K) reduction of a $Mg(Al,Ga)O_x$-, or Ga_2O_3-supported Pt catalysts in H_2 by x-ray diffraction. In comparative test reactions, a high Ga content (resulting in Pt content as low as 2 at.%) was demonstrated to decrease activity in favor of selectivity and coke deposition rate.[55] Similar effects are also demonstrated in a number of other studies addressing the catalytic dehydrogenation of alkanes.[56–58]

Iwasa et al. demonstrated that catalysts prepared by impregnation of ZnO, In_2O_3 or Ga_2O_3 with Pt or Pd show increased selectivity in methanol dehydrogenation and methanol steam reforming. This is ascribed to the presence of binary alloys, which are formed during reductive pretreatment at 773 K.[59, 60] Similar results were also found for systems created by impregnation of Ga_2O_3 with Pd. It was demonstrated that pretreatment in H_2 at temperatures between 623 and 773 K leads to the formation of the IMC Pd_2Ga and PdGa and to a remarkable increase in both conversion and

CO_2 selectivity in methanol steam reforming.[24, 61, 62]

Bimetallic catalysts consisting of Ga and Pd were also shown to be well applicable in the reverse reaction of the dehydrogenation; Schlögl et al. and Rupprechter et al. have taken strong efforts to examine the potential of different solid Ga_xPd_y IMC as catalysts primarily for the selective hydrogenation of alkynes to alkenes. The high selectivity of these catalysts in these reactions is ascribed to the isolation of active sites by increasing Ga content, and the suppression of Pd hydride formation, which leads to a decrease in activity towards hydrogenation of the ethylene C=C bond. [25, 63–72]

These examples have in common that the utilized catalyst is either prepared as alloy purposely, or an catalytically active alloy phase is formed in-situ by reductive pretreatment at elevated temperatures. As heterogeneous catalysis happens mediated by the surface of the catalytically active phase, the exact knowledge of the composition of the catalyst-gas interface under reaction conditions is of key relevance for understanding and optimizing the catalyst. For metallic multicomponent systems this also implies a precise understanding of the processes occurring during catalyst manufacturing, start-up and operation. The distribution of elements in a multi-metallic system, in particular in proximity to an interface, results from the complex interplay between segregation and ordering tendencies.[73] Depending on whether mixing of the elements is energetically favored, the binary system will show a tendency to surface segregation or even bulk phase separation, or to the formation of an ordered phase. In general, for a segregating system, the component with lower free surface energy will dominate the interface composition. Ordering tendencies on different length scales (long- and short-range order) can result from the energetic benefit of a periodic arrangement, and the latter can also be induced by an interface. For the three binary systems (Pt/Pd/Rh in Ga) examined in the scope of this thesis negative mixing enthalpies are reported for the whole composition range for the liquid constituents, and a pronounced tendency for ordering is manifested through multiple IMCs distributed over the whole phase diagram of the three systems. The local extrema, that is, minimum enthalpy of mixing in $\Delta_{mix}H^0$ vs. x_{TM} curves are found to decrease in the oder Rh: x = 0.5, $\Delta_{mix}H^0 = -64\,\mathrm{kJ\,mol^{-1}}$, Pt: x = 0.55, $\Delta_{mix}H^0 = -66\,\mathrm{kJ\,mol^{-1}}$ and Pd: x = 0.6, $\Delta_{mix}H^0 = -70\,\mathrm{kJ\,mol^{-1}}$.[74–78] Experimental surface energies are reported to decrease in similar order: Rh (Experiment: 2.659 and 2.700 $\mathrm{J\,m^{-2}}$, Theory: 1.002 $\mathrm{eV\,atom^{-1}}$ for fcc(111)), Pt (Exp.: 2.475 and 2.489 $\mathrm{J\,m^{-2}}$, Th.: 1.004 $\mathrm{eV\,atom^{-1}}$ for fcc(111)), Pd (Exp.: 2.003 and 2.050 $\mathrm{J\,m^{-2}}$, Th.: 0.824 $\mathrm{eV\,atom^{-1}}$ for fcc(111)).
If compared to the transition metals, Ga exhibits much lower values (Exp.: 0.881 and 1.100 $\mathrm{J\,m^{-2}}$, Th.: 0.376 $\mathrm{eV\,atom^{-1}}$ for bct(001))[79, 80], and is therefore expected to dominate the surface in a segregated binary alloy. In the row of examined transition metals, the trend to segregate to the surface will decrease in the order Rh, Pt, Pd according to mixing enthalpies and surface energies.[73, 81, 82]

2. Fundamentals

2.1. X-ray photoelectron spectroscopy

X-ray **P**hotoelectron **S**pectroscopy (XPS), also known as **E**lectron **S**pectroscopy for **C**hemical **A**nalysis (ESCA), is a technique based on the photoelectric effect, which was first observed and described by Hertz in 1887 [83]. In 1905, the observed effect was explained by Einstein [84]. The development of experiments utilizing photoemission to probe the physics of molecules, and solid state matter and its surfaces with high resolution by Siegbahn [85] were honored with the Nobel prize in physics in 1981 [86]. Since then, the technique, also due to technical progress, has matured and is in frequent use in many different fields of research.

2.1.1. The binding energy in XPS

The irradiation of samples by x-ray photons of energies $h\nu$ exceeding the sum of the binding energy E_b of a core-bound electron and the work function ϕ_S of the irradiated material will lead to the excitation of electrons into continuum states. The energy-level diagram of the photoemission process is shown in Figure 2.1.

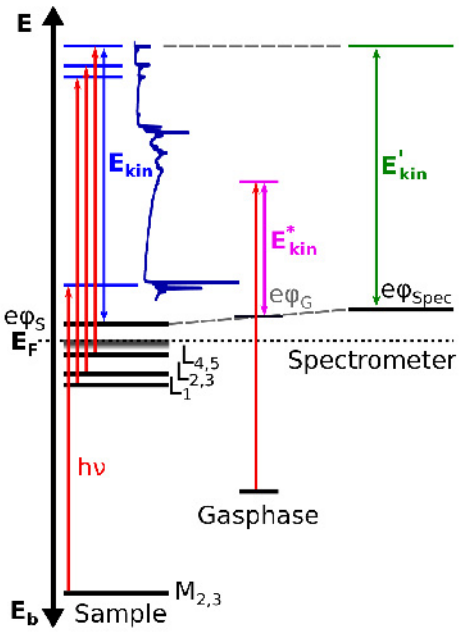

Figure 2.1.: Schematic representation of the photoionization process and photoelectron detection in an energy level diagram.

Due to energy conservation, the sum of initial state energy E_i – that is, the energy of the neutral N electron system – and $h\nu$ equals the sum of the energy of the final state – the ionized atom, that is, the N-1 electron system –, the kinetic energy E_{kin} of the free electron, and the work function of the irradiated material ϕ_S as given by equation (2.1).

$$E_i + h\nu = E_f + E_{kin} + \phi_S \tag{2.1}$$

In an XPS experiment, a current of photoelectrons will be detected as function of the electron kinetic energy. For display and discussion of acquired data, however, it is convention to display the photoelectron count-rate as function of the binding-energy. Following from equation (2.1), an expression for the binding energy E_b of the electron would be given by equation (2.2).

$$\begin{aligned} E_b &= h\nu - E_{kin} - \phi_S \\ &= E_f - E_i = -\varepsilon + E_{relax} \end{aligned} \tag{2.2}$$

The difference of final and initial state energies can be assumed to be equal to the negative Hartree-Fock energy of the core-bound electron ε, and the term denoted E_{relax} in equation (2.2), which accounts for relaxation of the electronic structure of the ionized source atom in response to core-hole formation, will be neglected. In the experiment, however, the difference between the actual final- and initial-state energy will be probed by detecting the emitted photoelectron as a function of its kinetic energy E_{kin}. Hence, mechanisms influencing the measured kinetic energy and thus the calculated binding energy are differentiated into so called final- and initial-state effects. Final state effects include for example the coupling to vibrationally excited states of molecules or phonons, plasmon-, shake-up- and shake-off excitations, multiplet splitting or differences in core-hole screening efficiency.[87] Among the initial-state effects, changes in the electron binding energy due to rearrangements in the local electronic structure by e.g. coordination chemistry of adsorbate molecules and surface atoms, or changes of the oxidation state of adsorbates and substrate atoms are of great importance for the surface chemist, as the photoelectron hereby functions as a probe for the chemistry of molecules and surfaces.

Samples are typically conductively connected to the spectrometer for the measurement. This leads to alignment of the Fermi-levels, which ensures a common reference energy for conductive samples and spectrometer, and will avoid charging of the sample. Differences in the work-functions of sample and spectrometer $\Delta\phi = e \cdot \Delta\varphi = e \cdot (\varphi_S - \varphi_{Spec})$, however, will lead to a contact potential, which will de- or accelerate the photoelectron to kinetic energy $E'_{kin} = E_{kin} + \Delta\phi$, shown in green in Figure 2.1. For the calculation of binding energies in the experiment, the contact potential therefore has to be taken into account as shown in equation (2.3).

$$\begin{aligned} E_b &= h\nu - E_{kin} - \phi_S \\ &= h\nu - E'_{kin} + (\phi_S - \phi_{Spec}) - \phi_S \\ &= h\nu - E'_{kin} - \phi_{Spec} \end{aligned} \tag{2.3}$$

Irradiated gas-phase atoms or molecules will emit photoelectrons with the local vacuum-level *floating* atop an external potential φ_G that is due to the potential drop between sample and spectrometer. A build-up of charge by photoionization of the gas phase may additionally shift this local potential. The kinetic energy E^*_{kin} of photoelectrons emitted by gaseous species, shown in magenta in Figure 2.1, may therefor vary with the position of the source atom between sample and spectrometer and sample positioning. Further, charging of the gas phase, or work-function changes of the sample induced by surface chemistry, which – due to Fermi-level alignment of sample and spectrometer – do not have an influence on the measured kinetic energy of photoelectrons of the solid sample will, however, alter the measured binding energy of core level signals of gas phase atoms or molecules.[88]

It is the convention to give and discuss binding energies of conductive solids referenced to the Fermi energy, while binding energies of gas phase species can only be given with respect to the local vacuum level.

2.1.2. Surface sensitivity in XPS

Within the three-step model of photoemission[87], the excited photoelectron will be transported to the surface and emitted into vacuum after excitation. Each of these steps contributes to the number of distinct features in the spectrum and the overall shape of the latter. While the features resulting from the first step, that is, the excitation, have been discussed as final- and initial-state effects before, the transport[89] to the interface is discussed in the following. Pronounced energy loss can result from extrinsic (in contrast to intrinsic, which would be the final state effect) excitation of phonon or plasmon modes, which produces sharp satellite features shifted to higher binding energy in the spectrum. Furthermore, particularly in metallic media, intra- and interband transitions can be excited. This multitude of (multiple) inelastic scattering events produces asymmetry in form of an unresolved, quasi-continuous pile-up of scattered electrons shifted towards the side of higher binding energy of every core level signal, which – along with bremsstrahlung radiation – defines the asymmetry of signals and the background observed in XPS measurements. Due to the typically low kinetic energy of photoelectrons in lab-based XPS, cross sections for inelastic scattering will be high, and photoelectrons will therefore strongly interact with the matter they are originating from, which is responsible for the surface sensitivity of the method.

The mean free path (MFP) of a particle, according to collision theory, is defined as the length λ a particle has to travel in a medium of targets with constant target density $n = {}^{N}/_{V}$ to undergo a single collision, as given in equation (2.4). Therein the interaction cross section σ quantifies the interaction probability between particle and target.

$$P(z) = \sigma n \int \mathrm{d}z = \sigma n \lambda = 1 \tag{2.4}$$

The change in intensity of a monochromatic particle beam dI within a path length dz will be proportional to the intensity $I(z)$ and the sum of the probabilities for m different processes prohibiting

the detection of the particle.

$$\int \mathrm{d}I = -I(z) \cdot \sum_m P_m(z) = -I(z) \cdot \sum_m \int n_m(z) \sigma_m(z)\, \mathrm{d}z \tag{2.5}$$

This expression can be solved to yield what is know as Lambert-Beer law.

$$I = I_0 \cdot e^{-\sum_m \int n_m(z) \cdot \sigma_m(z)\, \mathrm{d}z} = I_0 \cdot e^{-\sum_m \int \mu_m(z)\, \mathrm{d}z} \tag{2.6}$$

For quantitative XPS analysis, typically everything but inelastic scattering is neglected, and n as well as σ are assumed to be constant. Equation (2.6) then is reduced to the following:

$$I = I_0 \cdot e^{-z \cdot \sigma \cdot n} = I_0 \cdot e^{-z/\lambda} \tag{2.7}$$

where I/I_0 is the transmission along z, which is the effective path length, e.g. the thickness of an overlayer film, and λ is the energy-dependent inelastic mean free path (IMFP) of photoelectrons in the medium. Depending on the medium, different models for the IMFP are applied. If photoelectrons are attenuated by the presence of gas phase, as for example in a high-pressure XPS setup, the target density can be expressed by means of the ideal gas law, and the cross section for inelastic scattering of the photoelectron may be accessible in the form of tabulated data in literature.[90–94]

$$\lambda^{-1} = \frac{p}{k_B T} \cdot \sigma \tag{2.8}$$

If solid media are to be described, integration of the so called differential inverse inelastic mean free path DIIMFP, which quantifies the probability for inelastic interaction including specific extrinsic excitations like plasmon modes, over all possible momentum losses yields the inverse IMFP.[87, 89] A more general expression for the IMFP as function of atomic data and materials constants (mass density ρ, molar mass M, band gap energy E_g, number of valence electrons N_v), derived from fitting to experimental data and found to be in agreement with the latter within a RMS of 11 %, is reported by Tanuma, Powell and Penn and consequently called the TPP2-M equation [95].

$$\begin{aligned}
\lambda^{-1} &= \frac{E_p^2 \left[\beta \ln(\gamma E) - C/E + D/E^2\right]}{E} \\
\beta &= -0.10 + 0.944 \left(E_p^2 + E_g^2\right)^{-1/2} + 0.069 \rho^{0.1} \\
\gamma &= 0.191 \rho^{-1/2} \\
C &= 1.97 - 0.91U \\
D &= 53.4 - 20.8U \\
U &= N_v \rho / M = E_p^2 / 829.4
\end{aligned} \tag{2.9}$$

Within the energy range provided by the typical laboratory x-ray source, that is, up to 1253.6 and 1486.7 eV for the Mg and Al K_α line respectively, the IMFP will be found in the order of several nm. An estimate regarding the surface sensitivity in XPS is possible by defining the information depth

(ID, d_{info}) to correspond to the depth from where 95 % of the total signal are generated. It follows that $d_{info} \approx 3\lambda$ after solving equation (2.10).

$$\frac{I}{I_\infty} = \frac{I_0 \cdot \int_0^{d_{info}} e^{-z/\lambda}\,\mathrm{d}z}{I_0 \cdot \int_0^{\infty} e^{-z/\lambda}\,\mathrm{d}z} = 0.95 \tag{2.10}$$

2.1.3. Near-ambient pressure XPS

Combining equations (2.5) and (2.8), an expression for the attenuation of photoelectrons emitted by samples, which are exposed to elevated reactant pressures can be derived:

$$I = I_0 \cdot e^{-\int \sigma \cdot \frac{p(z)}{k_B T}\,\mathrm{d}z} = I_0 \cdot e^{-\frac{d_{eff}\sigma p_0}{k_B T}} \tag{2.11}$$

Where, if the pressure profile along z is unknown, and values for σ are available, d_{eff} can experimentally determined for different pressures p_0 of different gas-phase species.

2.1.4. Quantitative XPS

The total photoelectron current emitted by a sample will be influenced by geometry-, energy- or element-specific factors as given in equation (2.12).[96]

$$\begin{aligned} dI_{A,i} = \sigma_{A,i} D(E_{pass}) \int_{\gamma=0}^{\pi} \int_{\phi=0}^{2\pi} L_{A,i}(\gamma) \\ \cdot \int_{y=-\infty}^{\infty} \int_{x=-\infty}^{\infty} J_0(xy) T(xy\gamma\phi E_{A,i}) \\ \cdot \int_{z=0}^{\infty} N_A(xyz) \cdot e^{-\frac{z}{\lambda(E_{A,i})\cos(\vartheta)}}\, dz\,dx\,dy\,d\gamma\,d\phi \end{aligned} \tag{2.12}$$

Therein $\sigma_{A,i}$ is the photoelectric cross section, a function of the excitation energy $h\nu$ quantifying the probability to excite the transition i of atom A. $D(E_{pass})$ is the detector efficiency at a kinetic energy E_{pass}, the so-called pass energy of the hemi-spherical analyzer. $L_{A,i}(\gamma)$ is the angular asymmetry of the photoemission process. $J_0(xy)$ is the impinging photon flux, which is assumed to be z-independent within the probed volume of the sample due to the low information depth of photoelectrons. $T(xy\gamma\phi E_{A,i})$ is the detector's transmission efficiency. $N_A(xyz)$ is the density of atom A within the probed sample volume. $E_{A,i}$ is the kinetic energy of photoelectrons, according to equation (2.2). Photoelectrons that stem from certain depths z have a reduced probability to arrive at the detector compared to photoelectrons originating directly from the sample-vacuum interface due to inelastic scattering within the sample, hence the Lambert-Beer-type exponential. This includes the inelastic mean free path and effective path length $z/\cos(\vartheta)$ of the photoelectron leaving

sample medium at an angle ϑ relative to the surface normal, to account for attenuation of the photoemission signal from depths z by a covering layer of thickness $< z$. This lengthy equation is simplified to great extend by assuming negligibility of $L_{A,i}(\gamma)$ at an emission angle of $\gamma = 54.7^\circ$ relative to the incident x-ray beam, and a fixed, narrow acceptance angle of the electron analyzer.[97] For laboratory experiments, also the photon flux $J_0(xy)$ remains constant. Additionally, the efficiency of detection at invariant pass energies E_{pass}, as well as acceptance angle and spot-size will be determined by the spectrometer setup and are assumed to be constant. Further simplification can therefore be achieved when using relative intensities or reference measurements of pure elements for the quantification of element A or B in the mixture A_xB_y collected with the same instrument and setup. After analytically solving the remaining integral over z, assuming N_A to be constant (i.e. a homogeneous mixture of elements, or pure element), equation (2.12) breaks down to equation (2.13). Therein part of the physical quantities discussed above have been canceled out and only those that vary with choice of element, transition, emission angle or energy remain.

$$\frac{I_{A,i}^{exp}}{I_{A,i}^{ref}} = \frac{\sigma_{A,i} T(E_{A,i}) N_A^{exp} \lambda_A^{exp}(E_{A,i}) cos(\vartheta)}{\sigma_{A,i} T(E_{A,i}) N_A^{ref} \lambda_A^{ref}(E_{A,i}) cos(\vartheta)} \tag{2.13}$$

Consequently, to determine the ratio of elements A and B within a homogeneous mixture A_xB_y in accordance to equation (2.14) only few additional quantities have to be added to the experimentally determined intensities. Namely these are the electron inelastic mean free path and atom density of elements A and B within the reference and sample media.[96]

$$\frac{N_A^{exp}}{N_B^{exp}} = \frac{I_{A,i}^{exp} N_A^{ref} \lambda_A^{ref}(E_{A,i})}{I_{A,i}^{ref} \lambda_A^{exp}(E_{A,i})} \cdot \frac{I_{B,j}^{ref} \lambda_B^{exp}(E_{B,j})}{I_{B,j}^{exp} N_B^{ref} \lambda_B^{ref}(E_{B,j})} \tag{2.14}$$

If reference measurements are not available, tabulated values for the photoemission cross section [98, 99] can be used to quantify the relative atom densities of elements A and B according to equation (2.15). For, e.g. the Omicron EA125 hemispherical electron energy analyzer at a pass energy of 40 eV, $T \propto E_{kin}^{-1}$ is demonstrated to be a valid approximation for kinetic energies as low as 110 eV using the circular entrance slits, and as low as 450 eV using the rectangular entrance slits.[100]

$$\frac{N_A^{exp}}{N_B^{exp}} = \frac{I_{A,i}^{exp}}{\sigma_{A,i} T(E_{A,i}) \lambda_A^{exp}(E_{A,i})} \cdot \left(\frac{I_{B,j}^{exp}}{\sigma_{B,j} T(E_{B,j}) \lambda_B^{exp}(E_{B,j})} \right)^{-1} \tag{2.15}$$

Equations (2.13), (2.14) and (2.15) will fail to properly evaluate samples, which are inhomogeneous along the z-direction as for the analytical solution of equation (2.12) constant atom density N_A is assumed. Instead an approximation to the integral $\int N_A(z) \cdot e^{-z/\lambda(E_{A,i})cos(\vartheta)} dz$ in equation 2.12 in the form of equation (2.16) can be used to describe a structured system of n layers having equal thickness *d* and constant, element-unspecific atom density *N*, where then the atom density of species *a* is $N_{A,n} = N \cdot x_{A,n}$.[101] For this approximation, also negligible influence of the composition of layer *n* on λ is assumed, which is expected to be valid for a system comprising *A* different

minority species, and a single majority species *B*.

$$\begin{aligned}&\sum_{n=1}^{n_{max}} \int_{(n-1)\cdot d}^{n\cdot d} N\cdot x_{A,n}\cdot e^{-\frac{z}{\lambda_B(E_{A,i})cos(\vartheta)}}dz + \int_{n_{max}\cdot d}^{\infty} N\cdot x_{A,\infty}\cdot e^{-\frac{z}{\lambda_B(E_{A,i})cos(\vartheta)}}dz \\ =&\lambda_B(E_{A,i})cos(\vartheta)N\cdot\left[\sum_{n=1}^{n_{max}} x_{A,n}\left(e^{-\frac{(n-1)\cdot d}{\lambda_B(E_{A,i})cos(\vartheta)}}-e^{-\frac{n\cdot d}{\lambda_B(E_{A,i})cos(\vartheta)}}\right)+x_{A,\infty}\cdot e^{-\frac{n_{max}\cdot d}{\lambda_B(E_{A,i})cos(\vartheta)}}\right]\end{aligned} \tag{2.16}$$

The ratio of atoms A and B – as it would be determined from quantitative analysis of inhomogeneous samples using equation (2.15) – can then be calculated according to equation (2.17). Equation (2.17) was used for data discussed in Section 4.2.

$$\frac{N_A}{N_B}=\frac{\sum_{n=1}^{n_{max}} x_{A,n}\left(e^{-\frac{(n-1)\cdot d}{\lambda_B(E_{A,i})cos(\vartheta)}}-e^{-\frac{n\cdot d}{\lambda_B(E_{A,i})cos(\vartheta)}}\right)+x_{A,\infty}\cdot e^{-\frac{n_{max}\cdot d}{\lambda_B(E_{A,i})cos(\vartheta)}}}{\sum_{n=1}^{n_{max}} x_{B,n}\left(e^{-\frac{(n-1)\cdot d}{\lambda_B(E_{B,j})cos(\vartheta)}}-e^{-\frac{n\cdot d}{\lambda_B(E_{B,j})cos(\vartheta)}}\right)+x_{B,\infty}\cdot e^{-\frac{n_{max}\cdot d}{\lambda_B(E_{B,j})cos(\vartheta)}}} \tag{2.17}$$

Analogous to equation (2.13) and (2.16), an expression for the intensity of an overlayer of element A and thickness d, relative to the intensity of the underlying substrate of element B can be derived from equation(2.12):

$$\frac{I_{A,i}^{exp,d}}{I_{B,j}^{exp,d}}\cdot\frac{I_{B,j}^{ref}}{I_{A,i}^{ref}}=\frac{\sigma_{A,i}T(E_{A,i})N_A^{exp}\lambda_A^{exp}(E_{A,i})(1-e^{-d/\lambda_A^{exp}(E_{A,i})})}{\sigma_{B,j}T(E_{B,j})N_B^{exp}\lambda_B^{exp}(E_{B,j})\cdot e^{-d/\lambda_A^{exp}(E_{B,j})}}\cdot\frac{I_{B,j}^{ref}}{I_{A,i}^{ref}} \tag{2.18}$$

For Section 4.3, where A = B = Ga and i = j = Ga $2p_{3/2}$ or Ga 3d, the thickness of a Ga_2O_3 film formed on top of the metallic Ga substrate was calculated using expression (2.19), which is derived from equation (2.18). For this purpose the intensities of the oxidic $I_{i,ox}$ and metallic components $I_{i,met}$ derived from the deconvolution of Ga $2p_{3/2}$ and Ga 3d signals were used in combination with Ga atom densities calculated from mass density of Ga and Ga_2O_3, and IMFP values calculated using equation (2.9). Applicability of equation (2.19) was also demonstrated for Al_2O_3 films on Al [102].

$$d=\lambda_{i,Ga_2O_3}\cdot ln\left[\frac{I_{i,ox}\lambda_{i,Ga}N(Ga)_{Ga}}{I_{i,met}\lambda_{i,Ga_2O_3}N(Ga)_{Ga_2O_3}}+1\right] \tag{2.19}$$

Therein, $\lambda_{i,Ga/Ga_2O_3}$ denotes the IMFP of photoelectrons from core level i in metallic Ga and Ga_2O_3, and $N(Ga)_{Ga/Ga_2O_3}$ is the Ga atom density in pristine Ga and Ga_2O_3, respectively.

2.2. Plasmon loss satellites in Ga

All signals related to source atoms embedded in metallic Ga typically are accompanied by satellite features shifted by 10.3 and 14.4 eV with respect to the binding energy of the main signal. This is shown for Ga 3d and Pd 3d spectra in Figure 2.2.

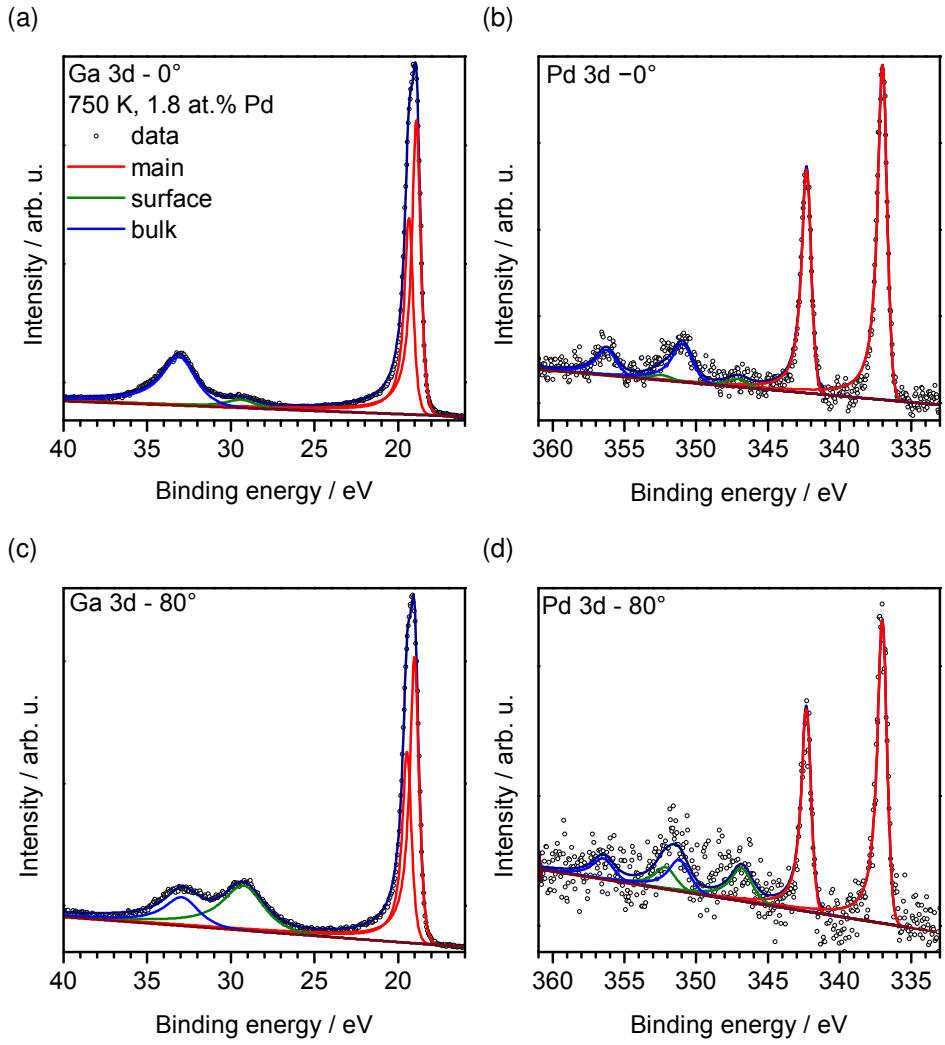

Figure 2.2.: Ga 3d and Pd 3d spectra collected in 0° ((a), (b)) and 80° ((c), (d)) emission. Along with the data, fitted models used in the evaluation are shown.

These loss features are ascribed to the excitation of bulk and surface plasmon modes in Ga [103], and they were therefore included in the quantitative analysis if necessary. In this case, the total intensity I_{total} was calculated from the intensity of the main signal I_{main} and the summed-up intensity of the two plasmon features I_{sat} in approximation as follows: $I_{total} = \sum_{n=0}^{\infty} I_{main} \cdot r^n \approx I_{main} + I_{sat} + I_{sat} \cdot r$ Therein r is the total intensity of the two satellite features with respect to the intensity of the main signal.

Table 2.1 shows experimentally determined, average values of r for the Ga $2p_{3/2}$, Ga 3d, Pd 3d,

Table 2.1.: Average relative satellite intensities r determined from the different probed core level signals on different instruments using Al K_α excitation.

	θ	Ga $2p_{3/2}$	Ga 3d	Pd 3d	Pt 4f	Rh 3d
DASSA	0°	0.33 ± 0.02	0.34 ± 0.03	0.32 ± 0.04	$0.27 \pm 0.03^{\dagger}$	
	80°	0.57 ± 0.04	0.51 ± 0.03	0.60 ± 0.08	$0.34 \pm 0.07^{\dagger}$	
GAP	0°	0.31 ± 0.01	0.33 ± 0.04	0.44 ± 0.08	$0.39^{\ddagger}$	0.27 ± 0.01

Pt 4f and Rh 3d signals. The given uncertainty represents the standard deviation. Please note that values of r for the Pt 4f signals are derived from only two measurements (DASSA, indicated by a superscript †), and a single measurement respectively (GAP, indicated by a superscript ‡), thus might have a higher error then indicated by the given error bars. The number of independent measurements for the Ga core levels typically were > 20. Values of r from spectra collected in 0° emission are smaller as compared to the ones observed for 80° emission data. This is also evident from Figure 2.2, where in addition a pronounced increase in the relative intensities of features ascribed to the surface plasmon excitation is visible for the 80° data. Within each of the two emission geometries, however, values of r for the different core level signals are found to agree within the experimental scatter. No significant temperature dependence of r was observed independent of the experimental geometry. Due to pronounced differences in information depth for 0° and 80° emission data in combination with different cross sections for bulk and surface plasmon excitation, different values of r are expected for the two emission geometries.[103–107]

The described loss satellites occur exclusively for signals assigned to the metallic Ga, and vanish e.g. for Ga or Pt signals ascribed to Ga or Pt atoms located in Ga_2O_3 as discussed in Section 4.3. For quantitative analysis the total intensities have thus to be corrected accordingly. For the data discussed in Section 4.2.1 and 4.3 the total intensities of Ga 3d and Pd 3d signals were corrected, whereas for the data shown in Section 4.2.2, values of r are assumed to be energy-independent, as reasoned by the data shown in Table 2.1, and quantitative analysis was conducted using the intensities of the main signals.

3. Instrumentation and experimental details

In the following, an overview of the two different instruments used for the acquisition of the data discussed in this thesis will be given. A detailed description of the two setups can be found in references [108, 109]. In addition, a brief description of sample geometries and preparation procedures will be given.

If not indicated differently, all data shown in the following chapters was collected using Al K_α radiation. Asymmetric combination of Duniach-Sunjic and Pseudo-Voigt functions, implemented as H()GL() in CasaXPS v.3.18, were fitted to asymmetric metal signals. Pseudo-Voigt functions, implemented as GL() were fitted to all other symmetric signals. Typically, linear baselines were subtracted to determine signal intensities from numerical integration of the data or the fitted functions, respectively.

3.1. The *GAP* instrument

For the collection of in-situ data at elevated pressures and temperatures, the so-called GAP setup was used. The instrument was custom-built by J. Pantförder at the chair of Physical Chemistry 2 of the University of Erlangen-Nuremberg in 2005. A detailed description and characterization of the instrument can be found in references [110] and [109]. The chamber comprises preparation and analysis chambers, which are connected by a transfer system, and are equipped with a separate manipulator and sample stage each. Load-lock and sample storage allow for frequent change of samples and storage of the latter under UHV conditions. The main feature of the analysis chamber, which enables the exposure of samples to elevated pressures, is the separation of chamber, excitation source (Specs XR50-HP, dual Al/Mg anode at 65° with respect to sample surface normal), and electron optics and detector (Modified Omicron EA125, 0° with respect to sample surface normal) into differentially pumped stages. These pumping stages are separated from each other by means of a x-ray transmissive Al-coated Si_3N_4 window in case of the excitation source, or by means of apertures limiting gas flow in case of chamber and electron optics and detector. In addition, the analysis chamber is equipped with a differentially pumped quadrupole mass spectrometer (QMS, Pfeiffer QME 200) connected to the second stage of the differential pumping scheme for the online analysis of gas composition. Attached to the preparation chamber are sputtergun, metal evaporators, a quartz crystal microbalance, a quadrupole mass spectrometer, and a low energy electron diffraction (LEED) instrument.

A photograph and description of the Ga evaporator added for this thesis, as well as drawings of additional, complementary apertures a_1 of minimum diameters of 0.6 and 1 mm can be found in Appendix B.

3.2. The *DASSA* instrument

For the collection of angle-resolved XPS data, a novel apparatus [108] featuring two electron analyzers (OMICRON Argus) oriented at an angle of 80° with respect to each other was used. The instrument uses a monochromatized Al K_α excitation source, oriented at an angle of 54.7° with respect to both analyzers, and is referred to as DASSA in text and illustrations. In addition, a He gas-discharge UV lamp for ultra-violet photoemission spectroscopy (UPS), and an ion source for low energy ion scattering (LEIS) experiments are mounted. The setup consists of two chambers, of which one is used for preparation, while the other one is used for the analysis, and a load-lock. The setup features a single manipulator, connecting preparation and analysis chamber. The preparation chamber is equipped with sputtergun, QMS, a dosing system used to backfill the chamber, and a sample storage.

3.3. Sample preparation

Metal single crystal surfaces, Pd(111), Pt(111) and Rh(111), were used as reference for quantitative analysis and the discussion of binding energies. These surfaces were cleaned by cycles of Ar^+ sputtering at 1 keV and high-temperature annealing, until no further contamination was observed in XPS. The long-range order was checked by LEED.

Catalyst or model samples examined within the scope of this thesis were prepared for XPS measurements as described in the following. Macroscopic droplets of Ga or the TM-Ga alloys were prepared by pouring liquid Ga (Merck, former Sigma-Aldrich, 99.99999 %) into W crucibles (Kurt Lesker GmbH, unknown purity) in air. Prior to preparation, the W crucibles were mounted to the sample support systems of the two chambers. The inner diameter of the W crucibles were 12 mm for the GAP setup, and 6 mm for the DASSA setup. If necessary, the crucibles were cleaned in concentrated hydrochloric acid to remove metallic impurities from spot-welding. Further cleaning was done by cyclic rinsing in acetone and iso-propanol in the ultrasonic bath for a minimum of 2 min each. Typically, the Ga mass was around 750 mg for samples examined in the GAP setup, and around 150 mg for samples examined in the DASSA setup. Transition metals were introduced by adding pieces of wire in air. After introduction to UHV, these samples were degassed, and heated to at least 750 K for prolonged times to decompose the native Ga_2O_3 film formed in air and facilitate alloying of the added metals. Carbonaceous impurities were removed by Ar^+ ion sputtering at 1 keV. Occasionally, significant carbonaceous impurities persisted on the sample surfaces, despite prolonged sputtering; in this case, new samples were prepared.

Type-K thermocouples were used to measure the crucible temperatures. These were spot-welded either to the outer bottom of the crucible in the GAP setup, or to the outer rim of the crucible in the DASSA setup. Samples were heated by direct current heating the W crucibles in the GAP setup, and radiative, field-free heating in the DASSA setup. Direct current heating in the GAP setup, in particular for high temperatures, induced static electric fields depending on temperature and sample geometry. These were never observed to significantly change collected intensities,

however, binding energies derived from high temperature spectra are corrected to compensate for these external potentials. As reference, typically binding energy of Ga 3d signals in pure Ga at 305 K was used.

The powder catalyst samples, all kindly provided by Dr. N. Taccardi from the work group of Prof. Dr. P. Wasserscheid at the chair of Chemical Reaction Engineering of the FAU Erlangen-Nuremberg, were attached to W foil using a silver/silica-based high temperature glue (plano-em) dispersed in water. The Pd-Ga/SiO_2 samples were then dried in air at 120 °C for at least 3 h to provide mechanical stability and sufficient electric conductivity of the glue. The Rh-Ga/Al_2O_3 catalyst samples were dried in air at room temperature, without any heating. After introduction to UHV, the samples were heated using resistive heating of the W foil, and temperature was controlled using a type K thermocouple spot-welded to the W foil. All powder samples were examined without further cleaning after introduction to UHV.

4. Results and discussion

This chapter will give an overview of both published, and unpublished results gained by the examination of samples related to binary Pt-Ga, Pd-Ga and Rh-Ga dehydrogenation catalysts. These range from the most complex systems, namely catalysts prepared on commercially available support materials, that is, Pd-Ga on porous glass or Rh-Ga on Al_2O_3 (Section 4.1) to the simplest model system, that is, droplets of pure Ga or alloys containing also small amounts of the transition metals Pt, Pd or Rh (Sections 4.2 and 4.3). Additionally, samples prepared by physical vapor deposition of Ga onto Au surfaces were examined, and the gained insights are discussed in Section 4.4. If indicated by a suffixed –P in the section title, published journal articles or drafts submitted or accepted for publication that are related to the discussed experiments can be found in Appendix A. In these cases, also the text was adapted from the published journal article [111–114].

4.1. Supported Pd/Rh-Ga bimetallic catalyst

In cooperation with the work groups of professors Wasserscheid, Görling, Hock and Peukert of the FAU Erlangen-Nuremberg, different variants of a novel catalyst material or concept, termed SCALMS for **S**upported **C**atalytically **A**ctive **L**iquid **M**etal **S**olutions, were synthesized, characterized and subjected to catalytic testing in the dehydrogenation of butane. Catalytic testing was done by J. Debuschewitz / Dr. N. Taccardi from the work group of Prof. Dr. P. Wasserscheid. Pd-Ga catalyst samples of different Ga/Pd ratios of Ga/Pd = 1 to 52 , that is, 50 to 2 at.% Pd were prepared by Dr. N. Taccardi as outlined in the following. Ga was deposited on the support by thermal decomposition of a $(Et_3)GaH_3$ precursor in ethereal solution. This was followed by galvanic displacement of Ga by Pd from a $PdCl_4$ solution. As support material TRISOPOR® with a pore diameter around 150 nm was used, which will be denoted porous glass or porous SiO_2 in this thesis for simplicity. Micron-sized metal particles rich in Ga are observed on the surface of the support in SEM micrographs. These are present after preparation, but also after reaction testing.

In a He-diluted (10:1) butane feedstock at 1.1 bar remarkable stability was demonstrated for on-stream times up to 20 h, with specific activity of the best-performing catalysts – those of minimum Pd content of 2 at.% – decreasing from 4.5 to 3 h^{-1}. Using a catalyst of 9 at.% Pd in an undiluted feedstock at 1.1 bar the specific activity of 15 h^{-1} was found to be constant for on-stream times up to 100 h. For high Ga/Pd ratios of the catalysts, also the selectivity for butene was found constant in the diluted feedstock, and it was demonstrated to increase to up to 80 % with increasing Ga/Pd ratio. Catalyst temperature in all these examples was 720 K, well above the liquidus temperature for the given stoichiometries. Similar experiments were conducted also with Rh-Ga catalysts supported on Al_2O_3, indicating similar stability at even increased specific activities compared to

the Pd-Ga systems in the dehydrogenation of propane. The comparison to "benchmark" catalysts, namely supported Pd and Pt, which suffered quick deactivation, revealed clear superiority of the novel catalyst materials. These are found to perform particularly well in terms of activity, selectivity and stability for high Ga/Pd or Ga/Rh ratios.[114]

The synergistic effect achieved by Ga addition is ascribed to the low average melting point of the mixtures resulting from a high Ga content and the presence of liquid bimetallic phases. These are assumed to maintain their activity under reaction conditions due to their liquid state that leads to the inhibition of coke formation. In this section the XPS data, that is, the spectroscopic characterization and quantitative analysis of different supported Pd-Ga and Rh-Ga catalysts will be shown and discussed. In later sections, experiments that attempt to shed light on the proposed explanation for the remarkable stability observed in catalytic testing of this novel class of materials are presented.

4.1.1. Pd-Ga on porous SiO_2 – P1

For two different samples of a catalyst with a nominal atomic Ga/Pd ratio of 21, corresponding to 4.5 at.% Pd with respect to Ga, the photoelectron spectra were recorded. Part of the recorded spectra, collected from one of the samples, are shown exemplarly in Figure 4.1.

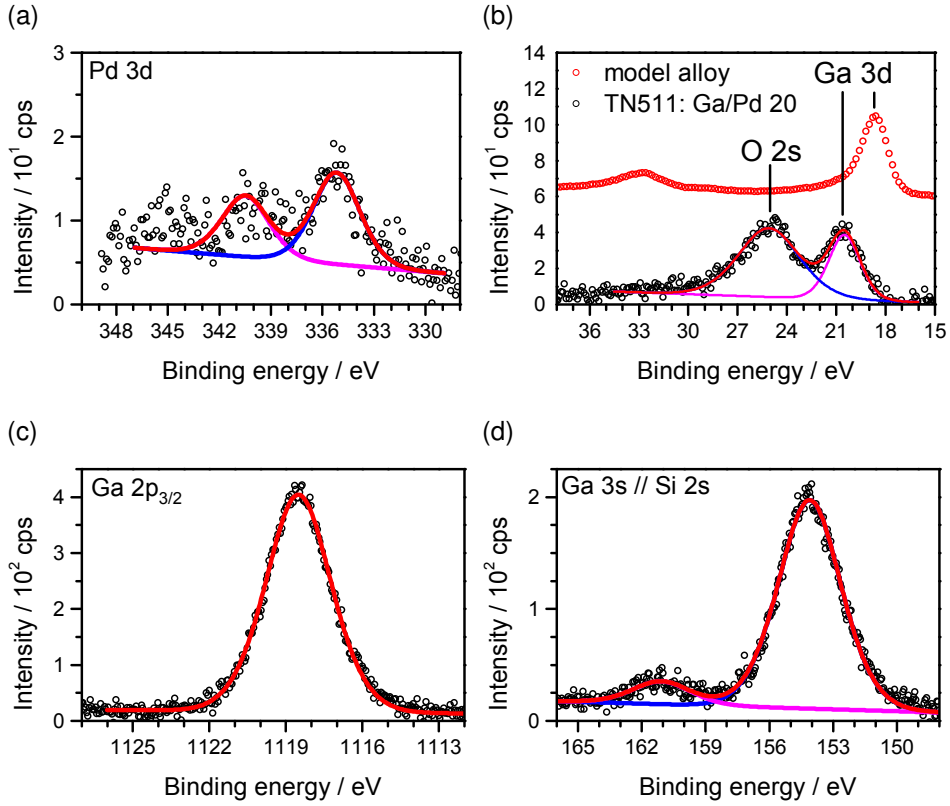

Figure 4.1.: Pd 3d (a), Ga 3d (b), Ga $2p_{3/2}$ (c) and Si 2s spectra (d) collected from a SiO_2-supported Pd-Ga catalyst of Ga/Pd = 21.

For the quantification, Si 2s, O 1s, Ga 3d and Pd 3d signals were analysed, and weighted according to equation (2.15). The binding energy scale is referenced to the binding energy of Si 2s/Si 2p in SiO_2 (154.1/103.2 eV [115]). The examined samples, as expected for insulating substrates, are prone to charging, and shifts up to 0.4 eV are observed in particular in temperature-dependent XP spectra (not shown) even after referencing to Si 2s/2p.

For the samples a consistent Ga loading of 13 ± 1 wt.% (nominal 4.9 wt.%) and a Pd loading of 1.5 ± 0.5 wt.% (nominal 0.4 wt.%) were determined. This corresponds to a molar Ga/Pd ratio of 14, that is 6.7 at.% with respect to Ga, which is in reasonable agreement with the synthesis. Deviations result from the low absolute amounts of Pd that lead to possible errors in quantification. Larger absolute values of the catalyst loading in the XPS analysis are expected as exclusively the surface of the sample is probed, whereas the nominal values are given with reference to the total mass of the porous SiO_2 support. Under the conditions of the XPS experiment, the Ga surface remained oxidized even up to 477 °C, as concluded from the absence of the metal-specific plasmon satellite of the Ga peaks or changes in the spectroscopic fingerprint. Binding energies of 20.5, 1118.5 and 335.1 eV are observed for the Ga 3d, Ga $2p_{3/2}$ and Pd $3d_{5/2}$ signals. Due to possible effects of charging, these binding energies are not given or discussed in P1, and are added here only for completeness.

4.1.2. Rh-Ga on Al_2O_3

Different catalyst samples of Al_2O_3-supported Ga/Rh alloys with a nominal Ga loading of 6 wt.% and Ga/Rh ratios of 16, 25, 58 and 88 (6, 4, 2 and 1 at.%) were examined using X-ray photoelectron spectroscopy (XPS) at room temperature and in UHV. Since the samples showed charging resulting in shifts of up to 7 eV, the binding energy scales are referenced to the binding energy of the Al 2p core level at 74.6 eV; this value was reported for Al_2O_3 in literature [116]. The quantitative analysis was performed in accordance to equation (2.15).

The Ga 3d spectra of the as-synthesized sample show one main Ga-related peak at 20.6 eV (red). Notably, this feature overlaps with the O 2s signal at 24 eV. An additional minor feature is located at 18.6 eV. In the Rh 3d region, only a single, spin-orbit-split doublet is observed, with the Rh $3d_{5/2}$/$3d_{3/2}$ peaks at 308.9 and 313.7 eV (red). The peaks have the expected splitting and intensity ratio of 4.75 eV and 3:2, respectively. The Ga 3d and Rh 3d spectra of the sample after the reaction show characteristic changes. In the Ga 3d region, the signal at 18.6 eV (blue) has significantly increased, to about 13 % of the total Ga 3d signal. The Ga 3d peaks at 20.6 and 18.6 eV binding energy are assigned to Ga_2O_3 and metallic Ga, respectively, in agreement with data shown in preceding sections. The increase of the metallic Ga content is also seen in the Ga $2p_{3/2}$ signals, where values of 7 % were found for the samples before and 14 % for the samples after the catalytic testing. These values agree with the Ga 3d-derived values, within the accuracy of the XPS analysis, and similar trends are observed for all examined samples. Considering the very different information depth of the Ga 2p ($E_{kin} \approx 370$ eV) and Ga 3d ($E_{kin} \approx 1460$ eV) photoelectrons, the equal ratios of reduced Ga to oxidized Ga indicate a homogeneous Ga_2O_3

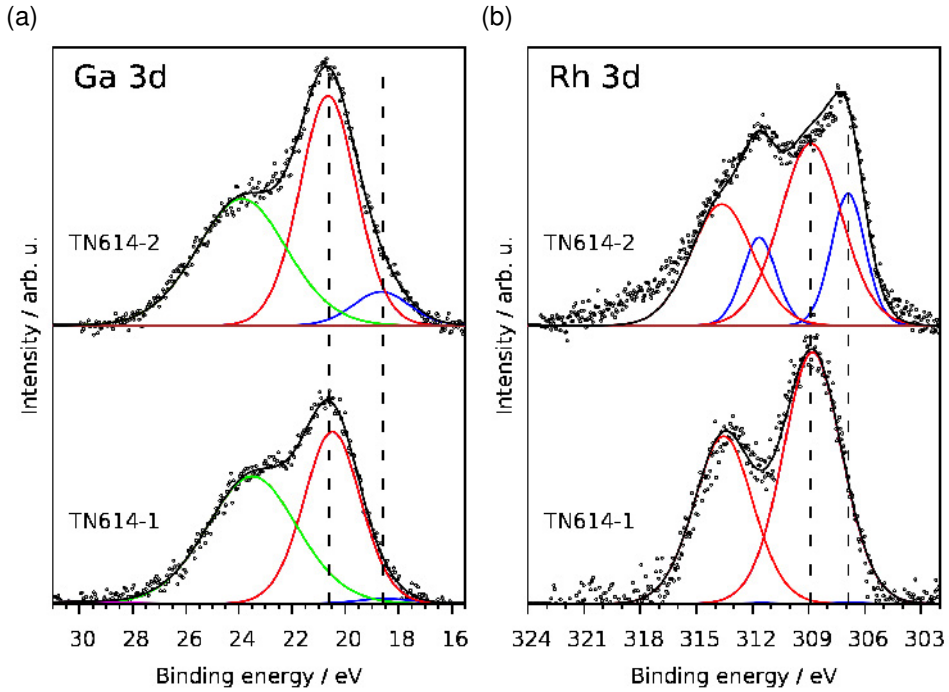

Figure 4.2.: Ga 3d (a), and Rh 3d spectra (b) of catalyst sample TN614. Suffixes indicate that the measurement was done directly after synthesis (-1) or after catalytic testing (-2).

distribution within the probed surface region of the catalyst particles. In the Rh 3d region, a new doublet at 306.9 and 311.7 eV (blue) is observed for the sample after the catalytic reaction, that is, at 2.0 eV lower binding energy than before the catalytic reaction. The binding energies are in reasonable agreement with the values of 307.4 and 312.2 eV) observed for a metallic Rh(111) surface. The Rh 3d doublet at 308.9 and 313.7 eV seen before the catalytic reaction is assigned to Rh_2O_3,or RhO_x respectively, according to literature. This assignment is based on reported values of 308.9 and 313.7 eV for bulk Rh_2O_3 [6], and shifts of 2.1 eV for bulk Rh_2O_3 [7] and 2.2 eV for oxidized Rh nanoparticles [8] relative to the reduced Rh species. The increase and appearance of the observed new Ga 3d and Rh 3d features is ascribed to the formation of metallic Ga and Rh species, that is, Ga, Rh, or Ga-Rh alloy phases, during the catalytic testing at elevated temperatures in the reductive environment of the reactor. Next, we have determined the Ga/Rh ratios of the various samples. This was done by assuming a homogeneous distribution of Rh in Ga, and summing up the oxidic and metallic components in Ga 3d and Rh 3d spectra. The Ga/Rh ratio of all examined samples prior to reaction is determined to 4 ± 1. Notably, this ratio is almost identical for these catalyst samples, although they have significantly different nominal Ga/Rh ratios. After reaction, the Ga/Rh ratio increased to values between 4.7 and 6.6, that is, by 30 to 70 % without any obvious systematic dependency on nominal values for the catalysts of nominal Ga/Rh ratio 16, 25 and 58. For the catalyst of nominal Ga/Rh ratio of 88 and increase in Ga/Rh ratio to 80, corresponding to an increase by 470 %, is observed. This indicates a redistribution of Ga or Rh during catalytic testing, which results in a more Ga-rich surface. Assuming a homogeneous dis-

tribution of all present elements, the weight loading of Ga prior to catalytic testing is calculated to be 18 ± 4 wt.% and the weight loading of Rh to be 6 ± 1 wt.%. The pronounced difference to the much lower nominal values is attributed to an accumulation of Ga and Rh in the surface-near region that is probed by XPS, and is therefore expected for a supported catalyst.

4.2. Angle-resolved photoemission spectroscopy of Pt/Pd/Rh-Ga alloys

As discussed in the introduction, for alkane dehydrogenation the most commonly utilized catalyst is Zn or Sn promoted Pt. Also for the Pd-Ga and Rh-Ga catalysts, as demonstrated in the preceding section, metallic binary phases are expected to play a significant role in applications. Such combination of different elements into a novel dehydrogenation catalyst provides the opportunity to optimize performance and adapt the catalyst to the demands imposed by the reaction conditions. The efficiency of Pt-Sn catalysts is explained by a combination of different effects, including also the stabilization of the active phase, which prevents sintering ,and the reduction of support-acidity needed for coke formation. Along with electronic effects, also the structure of the interface is of particular importance, as it defines the surface chemistry responsible for the catalytic efficiency of the active phase. For the supported Pt catalysts, Sn addition has been shown to increase selectivity towards the dehydrogenated product by increasing the dispersion. This is understood in terms of the lateral distribution and mutual proximity of active centers in the interface, which will alter so-called ensemble effects in structure-sensitive reactions. The dehydrogenation of acyclic alkanes, contrary to C–C bond breaking and forming reactions such as isomerization, cyclization or coke formation, typically is found being particle size-insensitive. This implies that a single active center might be able to catalyze the reaction, and the dilution of active centers is expected to increase selectivity. General consensus, however, also is that the dehydrogenation of acyclic alkanes follows an inverse Horiuti-Polanyi mechanism. This implies that either at least three active centers or efficient means for transport and recombinative desorption of hydrogen have to be present to enable the dehydrogenation to occur.[49, 117]

In a highly dynamic system, such as the discussed Ga-based bimetallic catalysts, also the distribution of the elements along the surface normal – in particular under reaction conditions – will influence efficiency, as it may limit the availability of active centers at the surface. Thus, to clarify the composition of the metallic alloys as function of the temperature, and to reveal possible inhomogeneities along the surface normal, angle-resolved XPS measurements were conducted. Model Pt/Pd/Rh-Ga alloys typically having a transition metal content less than 2 at.% were examined at temperatures between room temperature and 850 K. For all examined alloys, phase-separation leading to the formation of transition metal-rich IMCs and thus a depletion of the liquid bulk, is observed. Furthermore, for all the examined transition metals, a surface depletion, that is, Ga segregation to the interface is observed. Transition metal depletion of the surface is found to more pronounced in the order Pd to Pt to Rh. In case of Pd-Ga, the spectroscopic data discussed in the following Section 4.2.1 could successfully be compared in quantitative manner to results of molecular dynamics simulations done by J. Erhard in the workgroup of Prof. Dr. A. Görling. These findings are able to explain the resiliency towards coke formation by a minimized concentration of active centers in the interface and suggest a mechanism based on the limited and only short-termed availability of active centers at the interface.

4.2.1. ARXPS of Pd-Ga alloys – P2

Spectra of the Ga $2p_{3/2}$, Ga 3d, Pd 3d, O 1s and C 1s levels were collected for bimetallic samples of 0.8 and 1.8 at.% Pd at temperatures up to 850 K in 0° and 80° emission angle. For a sample of 4.7 at.%, complementary data was collected at the same temperatures in 0° exclusively. Typical measurements in the Ga 3d and Pd 3d region are shown in Figure 4.3 (a) and Figure 4.3 (b) for the sample with a nominal Pd content of 1.8 at.% Pd. For both emission angles, a strong increase of the Pd 3d peaks with increasing temperature is observed, while the Ga 3d peaks remain unchanged (within a standard deviation of 2 %). For all examined temperatures, the Pd 3d intensity at 80° is smaller than at 0° emission. The overall Pd 3d signal increase is accompanied by a systematic shift to lower binding energy by up to –0.5 eV (337.1 to 336.6 eV). No such shifts occur in the Ga core levels. The binding energy of the Pd $3d_{5/2}$ signals of the Ga alloys is larger by 1.0 to 1.5 eV due to the Pd-Ga interaction, as compared to the Pd(111) surface. Similar chemical shifts, due to interaction of the transition metal with Ga in Ga-rich matrices have been reported for various Pd-Ga intermetallic compounds (0.9 to 1.5 eV)[66, 69, 72].

From the quantitative analysis of the total signal intensities, the Pd concentration of the sample within the information depth of XPS was determined. As already evident from the spectra in Figure 4.3, the Pd surface concentration is strongly dependent on temperature, and there is also a pronounced systematic difference between Pd surface concentrations determined from 0° and 80° emission.

Pd concentrations x_{Pd} are plotted as function of the sample temperature for three different nominal Pd concentrations in Figure 4.4. Data obtained exclusively in 0° emission is shown in Figure 4.4 (a), while in Figure 4.4 (b) temperature-dependent data collected from a mixture of 1.8 at.% in 0° and 80° emission is shown exemplarily. We will focus on data collected in 0° in the beginning to discuss the observed temperature-dependence. For the 4.7 at.% mixture (black circles) it is evident that within temperatures of 630 to 850 K a temperature-independent Pd concentration of 4.7 ± 0.2 at.% is found. For the 1.8 at.% Pd mixture an average Pd concentration of 1.79 ± 0.03 at.% Pd is observed within a temperature range of 600 to 750 K, while for the 0.8 at.% Pd mixture the Pd concentration between 500 and 750 K is 0.73 ± 0.05 at.%. These average values are depicted in Figure 4.4 as dotted lines, along with error bars that represent their standard deviation. The average values of the Pd concentration obtained from XPS at 0° are in very good agreement with the bulk Pd concentration of the samples as determined from the weight-in (4.7 at.%), or standard-calibrated atom emission spectroscopy analysis (0.79 ± 0.01 and 1.83 ± 0.01 at.% Pd). In case of the 4.7 at.% mixture below 630 K a strong decrease of the measured Pd concentration occurs. For the 1.8 at.% Pd mixture, below 600 K, the Pd surface concentration as determined from the 0° as well as the 80° data decreases with decreasing temperature, as evident from Figure 4.4 (b). The observation of Pd depletion below a certain threshold temperature, which is increasing with Pd bulk concentration, is explained by a phase transition from the pure liquid phase to a two-phase system. The latter consist of a Pd-rich, solid intermetallic compound Ga_5Pd within a liquid Pd-Ga alloy. The formation of solid, Pd-rich crystallites in the

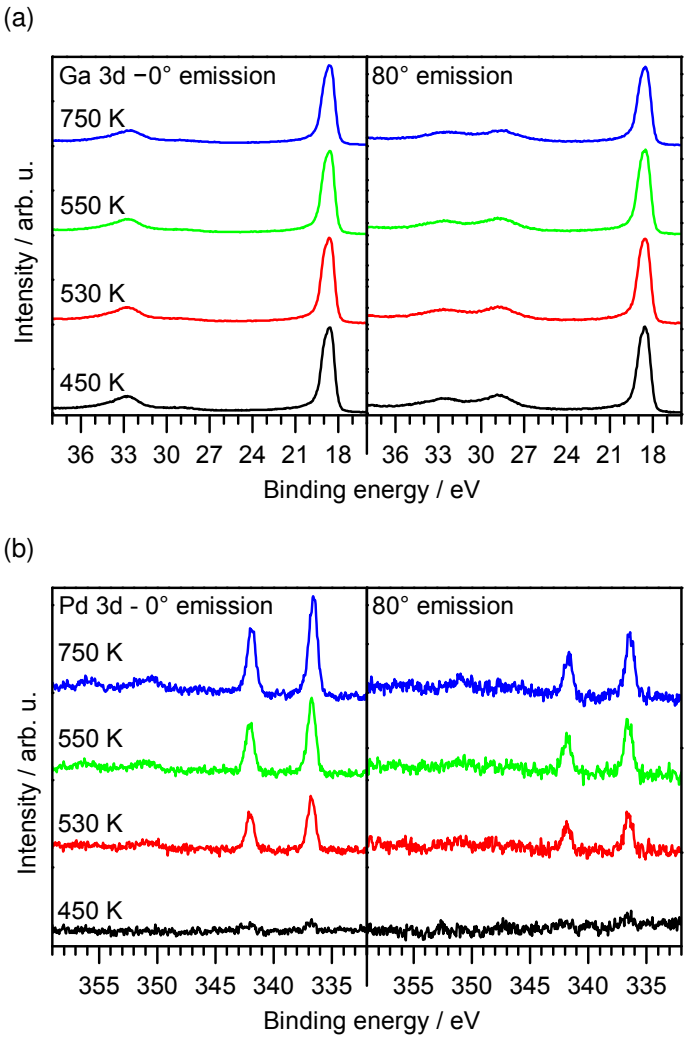

Figure 4.3.: Ga 3d (a) and Pd 3d spectra (b) collected at 0° and 80° emission, for the sample with a nominal Pd content of 1.8 at.% Pd. All data collected in 80° emission was scaled by a constant factor actor of 2.4 to normalize Ga 3d signal intensity.

liquid bulk leads to a Pd depletion of the remaining liquid alloy probed by XPS.

An occasional formation of Pd-rich crystals on the surface of the liquid phase can indeed be visualized by XPS-imaging, and is visible to the human eye. This provides further evidence of a phase separation observed in the temperature-dependent data. As the probed areas slightly differ in the two emission geometries, the formation of Pd-rich crystallites could lead to inconsistencies or increased scatter in the temperature-dependent data. This is, for example, observed at a temperature of 420 K, where the detected intensity in 0° emission is increased in contrast to the expected trend.

The average Pd concentration determined from the 80° data of the 1.8 at.% mixture, shown as blue circles in Figure 4.4 (b), between 600 and 750 K is 1.29 ± 0.07 at.%. For the 0.8 at.% mixture (data not shown) between 500 and 750 K a concentration of 0.49 ± 0.11 at.% is found. Notably, in the complete temperature range, a constant average ratio of $x_{Pd}(80°)/x_{Pd}(0°) = 0.77$ is observed

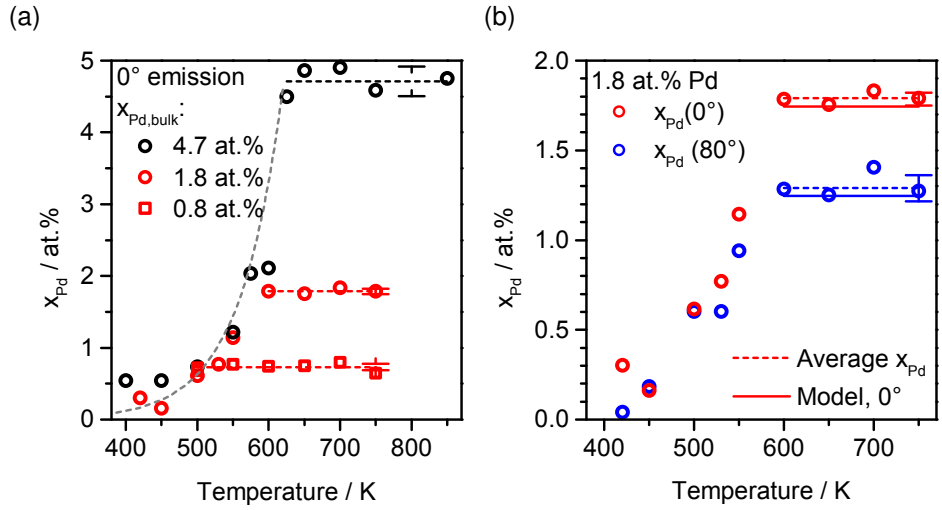

Figure 4.4.: Atomic Pd fraction plotted as function of temperature. Data collected exclusively in normal emission is shown in (a), whereas data collected in the ARXPS experiment, that is in 0° and 80° emission, is shown in (b).

(although scatter increases for low Pd surface concentrations), independent of temperature and bulk Pd concentration. As the measurement at 80° is much more surface sensitive than at 0°, the observed ratio is due to a surface depletion of Pd, which is independent of the temperature, that is, also independent of the the bulk phase transition.

Complementary DFT-MD simulations were done by J. Erhard from the workgroup of Prof. Dr. A. Görling at the chair of Theoretical Chemistry 2 of the FAU Erlangen-Nuremberg. These showed that the Pd and Ga distribution in a Pd-Ga alloy of 10 at.% Pd follows a damped oscillatory behavior, schematically shown also in Figure 4.5, with a minimum probability to find Pd in the first Ga layer, and a maximum probability to find Pd in the second Ga layer.

We used the results of the ICP-AES analysis, that is, the bulk Pd concentration $x_{Pd,bulk}$, and the MD simulation as input for a simple model of n rigid layers with varied Pd_aGa_b composition (a + b = 1), to approximate an inhomogeneous Pd depth-distribution function by a staircase function. The atomic fraction of Pd, as it would be determined in 0°/80° emission within the experiment, is calculated by summing up the contributions from layer n to the total signal of Pd and Ga, weighted with their molar fractions in the nth layer and the corresponding damping to the overlaying PdGa layers, in accordance to equation 2.16. In the model, we used the distribution of Pd as obtained from a staircase approximation to the MD results with respect to the bulk value of the respective Pd-Ga alloy. This results in values for the Pd atomic fraction $x_{Pd,n}$ of the n-th layer of $x_{Pd,1} = 0 \cdot x_{Pd,bulk}$,$x_{Pd,2} = 1.4 \cdot x_{Pd,bulk}$ and $x_{Pd,3} = 1.2 \cdot x_{Pd,bulk}$. The Pd concentrations x_{Pd} expected from quantitative analysis of 0° and 80° emission data are indicated as solid red and blue lines in Figure 4.4 (b), and show excellent agreement with the experimental data collected from the 1.8 at.% mixture. Please note that other models, such as the Langmuir-McLean-Theory[73, 118] describing segregation of a single monolayer, and an asymptotical increase to the bulk Pd con-

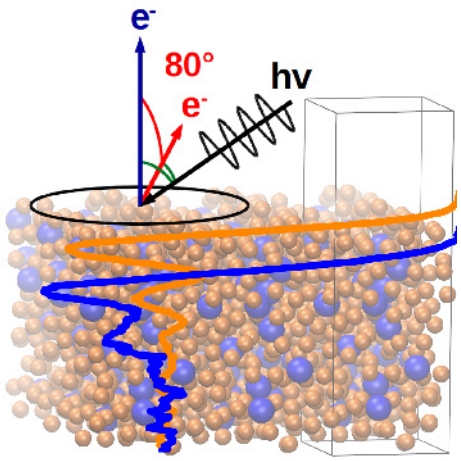

Figure 4.5.: Schematic representation of Ga (orange) and Pd (blue) distribution and the photoemission experiment from an artists perspective. The distribution curves are arbitrarily scaled for display. Shown is also a snapshot image of the supercell used in the MD simulation, which was kindly provided by J. Erhard along with the distribution curves of Ga and Pd. The shown figure was used as graphical abstract in article P2.

centration would also lead to a satisfying fit to the data. Please note that all these models agree on the fact that the first layer is Pd depleted. Using the enthalpies of vaporization of elemental Ga and Pd as a measure for interatomic bond strength, an estimation of possible surface segregation in binary alloys is possible.[119] As the enthalpy of vaporization of Ga is lower compared to Pd [120, 121], Ga segregation to the interface is minimizing the energy due to coordinatively unsaturated interface atoms, and Ga segregation is therefore indeed expected. This is also expected based on the surface energies discussed in Chapter 1.

In conclusion, in combination with DFT-MD, evidence for the layered structure formed by interfacial stratification and segregation of Ga in liquid Pd-Ga alloys is provided. Quantitative agreement to XPS data also provides evidence for the discussed Pd distribution – a surface depletion, and subsurface enrichment in the second and third layer.

4.2.2. ARXPS of Rh/Pt-Ga alloys

Complementary to the results discussed in Section 4.2.1, also Pt-Ga and Rh-Ga alloys were examined in angle-resolved XP (in 0° and 80° emission) experiments. Collected ARXPS data is supplemented with temperature-dependent data measured at higher temperatures in 0° emission exclusively. For quantitative analysis reference measurements of pure Ga, and clean Pt(111) and Rh(111) surfaces were used. In case of Pt-Ga, samples with a nominal content of 0.7 and 1.8 at.% Pt were examined. In Figure 4.6 (a) the results of quantitative analysis of Ga 3d and Rh 3d signals, that is, the atomic fraction of Pt x_{Pt}, is shown as function of temperature. For both mixtures, the Pt content initially is found to increase with increasing temperature. For the 1.8 at.% mixture, a constant Pt concentration of 1.9 ± 0.1 at.% is observed at temperatures above 760 K. In case of the 0.7 at.% mixture, a constant Pt concentration of 0.5 ± 0.1 at.% is observed at temperatures above 700 K. Similar to what has been discussed for the Pd-Ga alloys, the observed temperature-dependence is ascribed to a phase transition, that is, the melting or solidification of the solid IMC Ga_6Pt. Formation of the latter, at temperatures below the liquidus temperature, will lead to Pt depletion of the remaining liquid phase. Examination of the data collected in ARXPS experiments for a mixture of nominally 1.8 at.% Pt in 0° and 80° simultaneously, which is shown in Figure 4.6 (b), again reveals behavior as observed for the Pd-Ga alloy: The ratio $x_{Pt}(80°)/x_{Pt}(0°) = 0.72$ is found to be temperature-independent, and indicates an interfacial depletion of Pt.

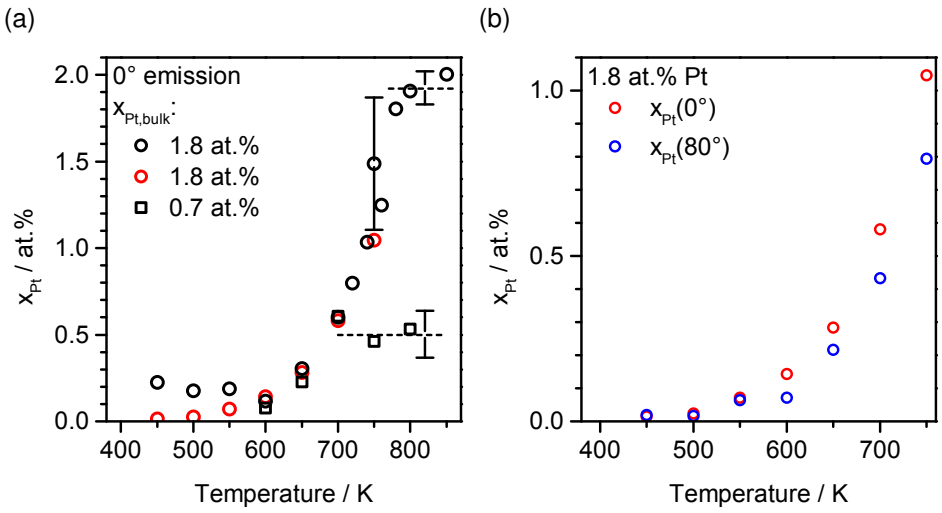

Figure 4.6.: Atomic Pt fraction plotted as function of temperature. Data collected exclusively in normal emission is shown in (a), whereas data collected in the ARXPS experiment, that is in 0° and 80° emission, is shown in (b).

Experiments were conducted with Rh containing Ga samples having a Rh content of 1.2, 1.8 and 2.0 at.%. The result of the quantitative analysis of the Ga 3d and Rh 3d core level signals collected in 0°, that is, the atomic Rh fraction x_{Rh}, is plotted as function of temperature in Figure 4.7 (a). Data collected in 0° and 80° emission simultaneously is shown in Figure 4.7 (b). Apparently, only for the sample of nominal Rh content of 1.2 at.% a temperature exceeding the

liquidus-temperature was achieved. For this sample, the average Rh concentration from quantitative analysis is 1.3 ± 0.1 at.% at temperatures above 800 K. For the 1.8 and 2.0 at.% mixtures, a temperature-independent Rh concentration could not be observed within the examined temperature-range. As for the Pd-Ga alloys, the nominal bulk Rh concentration of the samples was confirmed by standard-calibrated ICP-AES (N. Taccardi). When comparing data collected in 0° and 80° emission, surface Rh depletion, that is an average $x_{Rh}(80°)/x_{Rh}(0°) = 0.63$ is found, if considering the datapoint at 600 K an outlier.

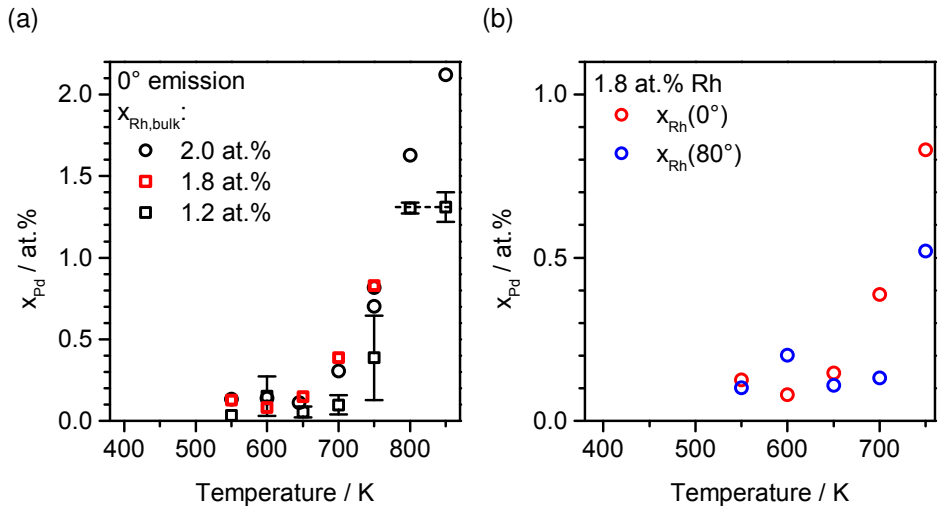

Figure 4.7.: Atomic Rh fraction plotted as function of temperature. Data collected exclusively in normal emission is shown in (a), whereas data collected in the ARXPS experiment, that is in 0° and 80° emission, is shown in (b).

By comparison of data collected from the different Pd/Pt/Rh-Ga alloys of 1.8 at.% of the transition metal in Ga it is evident that the liquidus temperatures, as derived from the temperature-dependent quantitative analysis of the surface composition in 0° emission, are found to increase in the order of Pd < Pt < Rh (620, 760 and >850 K). This is, despite significant differences in absolute temperatures, in line with the trend observed in liquidus temperatures crudely estimated from published phase diagrams (410, 500 and 810 K).[74, 75, 77, 78] The observed strong deviation might be related to undetected impurities or the presence of the liquid-solid (Ga-W) or liquid-vacuum interface. Furthermore, for the three examined transition metals an increasing trend to surface-depletion quantified by means of the $x_{Rh}(80°)/x_{Rh}(0°)$, which is found to decrease in the order Pd > Pt > Rh (0.77 > 0.72 > 0.63) is observed. This corresponds to an increase in Ga segregation and is found to be in qualitative agreement with the enthalpy of mixing decreasing in the order Rh-Ga, Pt-Ga, Pd-Ga, and with the surface energy decreasing in the order Rh,Pt,Pd.[74–80] Corresponding values are given and discussed in Chapter 1.

It is to mention that in contrast to the Rh-Ga system, where the Rh $3d_{5/2}$ binding energy of the liquid alloys in the examined compositional range is found to be 307.3 eV, which is in agreement with the binding energy of 307.4 eV observed for the clean Rh(111) surface, shifts of the Pt 4f

and Pd 3d core level signals are observed for the liquid phases of the Pt-Ga and Pd-Ga systems. These shifts are found to be of similar magnitude and agree qualitatively in terms of temperature-dependence. Shifts in the Pd 3d and Pt 4f core level signals, relative to the corresponding, clean (111) surfaces, are shown in Figure 4.8 as function of the sample temperature. The observed shifts are ascribed to the transition metal-Ga interaction, and they are therefore interpreted to be due to the changes in the composition of the liquid phase, induced by phase-separation upon changing temperatures. An increase in binding energy is observed for a decreased content of the transition metal in the liquid phase. To understand the exact nature and origin of this observation, ab initio calculations of binding energies might be helpful.

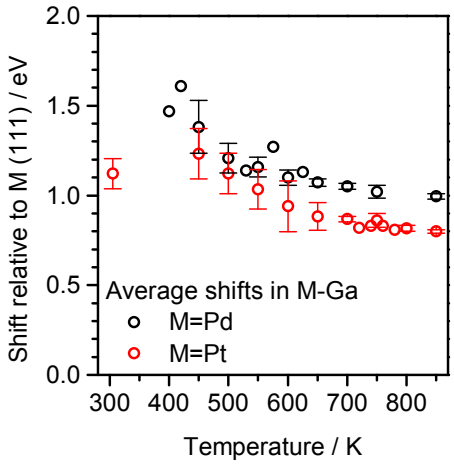

Figure 4.8.: Pd 3d and Pt 4f core level binding energy shifts observed from liquid alloys. Shifts are given with respect to the corresponding (111) surface and are shown as function of the sample temperature.

For solid Pd-Ga IMC similar shifts have been reported and were explained by electron transfer into Pd 4d states, resulting in increased Pd 3d core hole shielding and thus decreased final state screening.[72] These shifts appear to be linearly increasing with Ga content in the alloy material and a crude extrapolation to Pd contents below 5 at.% would yield shifts of approximately 2.1 eV; clearly the shifts observed for the liquid Pd-Ga alloys can not exclusively be ascribed to the nominal stoichiometry. Extrapolation of the reported data to the stoichiometry of the IMC Ga_5Pd results in shifts of approximately 1.7 eV. This is in line with shifts up to 1.6 eV observed for the Pd-Ga alloys at low temperatures around 400 K, indicating a possible contribution by solid IMC particles to the detected signal at this temperature. Please note that at the low temperatures, however, the discussed signals are close to the limit of detection, and show a rather high uncertainty in binding energy, which is indicated by error bars in Figure 4.8.

4.3. Oxidation of Pt/Pd-Ga alloys

As described in the introduction, the regeneration of dehydrogenation catalysts by burning off formed coke, is a frequent necessity in all the reviewed commercially applied processes. Furthermore, Ga is sensitive to molecular oxygen, and oxides formed from traces of oxygen in the feedstock will wet the surface of the Ga-based bimetallic liquid phase potentially influencing the catalytic process. This motivated the examination of the Pt/Pd-Ga model alloys response to exposure to molecular oxygen at pressures up to 1 mbar and temperatures up to 550 K. The examined alloys had transition metal contents of less than 2 at.% for both elements. Ga_2O_3 formation is observed, and growth of wetting films of thickness up to 37 Å was monitored in-situ. Pt is found to be incorporated into the formed Ga_2O_3 film with a constant stoichiometry of $x_{Pt} = 5.5 \pm 1.5\,\text{at.}\%$ with respect to Ga^{II} in Ga_2O_3 independent on the bulk concentration. This corresponds to a net enrichment of Pt at the surface. Contrary Pd is not incorporated into the newly formed Ga_2O_3 film, but a slight enrichment at the metal-oxide interface in response to initial stages of oxide growth is apparent, which is then followed by a decrease in the apparent Pd content ascribed to attenuation of the Pd 3d signals used for the quantitative analysis by the growing Ga_2O_3 overlayer. The gathered insights show, that for both systems, the presence of oxygen in the form of Ga_2O_3 leads to an enrichment of the active species at the surface. In case of the Pd-Ga system, however, the observed behavior also indicates a potential deactivation route in case the rate of Ga_2O_3 formation exceeds the rate of competitive processes like oxidative dehydrogenation or oxidation of hydrocarbons.

4.3.1. Oxidation of Pt-Ga – P3

Pure Ga, and alloys of 0.7 and 1.8 at.% Pt were exposed to molecular oxygen at pressures of 3×10^{-7}, 3×10^{-3} and 1 mbar, at sample temperatures of 300, 450 and 550 K. In all cases, the formation of Ga oxide occurs. Figure 4.9 exemplifies the data of an experiment for a Pt-Ga alloy with a Pt content of 1.8 at.%, conducted at 550 K and 3×10^{-7} mbar O_2.

Spectra plotted as blue and red lines were acquired in UHV before and after oxidation, respectively, and spectra plotted as grey lines were collected during exposure to 3×10^{-7} mbar O_2. The peaks of metallic Ga are located at 1117.0 and 18.9 eV for Ga $2p_{3/2}$ and Ga 3d, respectively. The formation of Ga oxide is reflected by the development of additional components at 1119.0 eV in the Ga $2p_{3/2}$ region (Figure 4.9 (a)) and at 20.9 eV in the Ga 3d region (Figure 4.9 (b)). These components are shifted by + 2.0 eV relative to the metallic components in both the Ga $2p_{3/2}$ and Ga 3d region. In addition, we also observe a peak at 531.6 eV in the O 1s region, as a result of the oxidation. Interestingly, for the alloy samples, we find a considerable increase of the Pt 4f signals, shown in Figure 4.9 (d), during oxidation, which occurs simultaneously to the increase in oxide-related Ga 3d or O 1s components.

The quantitative analysis of the integrated Ga 3d and O 1s peak areas yields an average stoichiometry of $Ga_2O_{3.2\pm0.5}$ for the formed oxides, and the observed binding energies in the Ga 2p

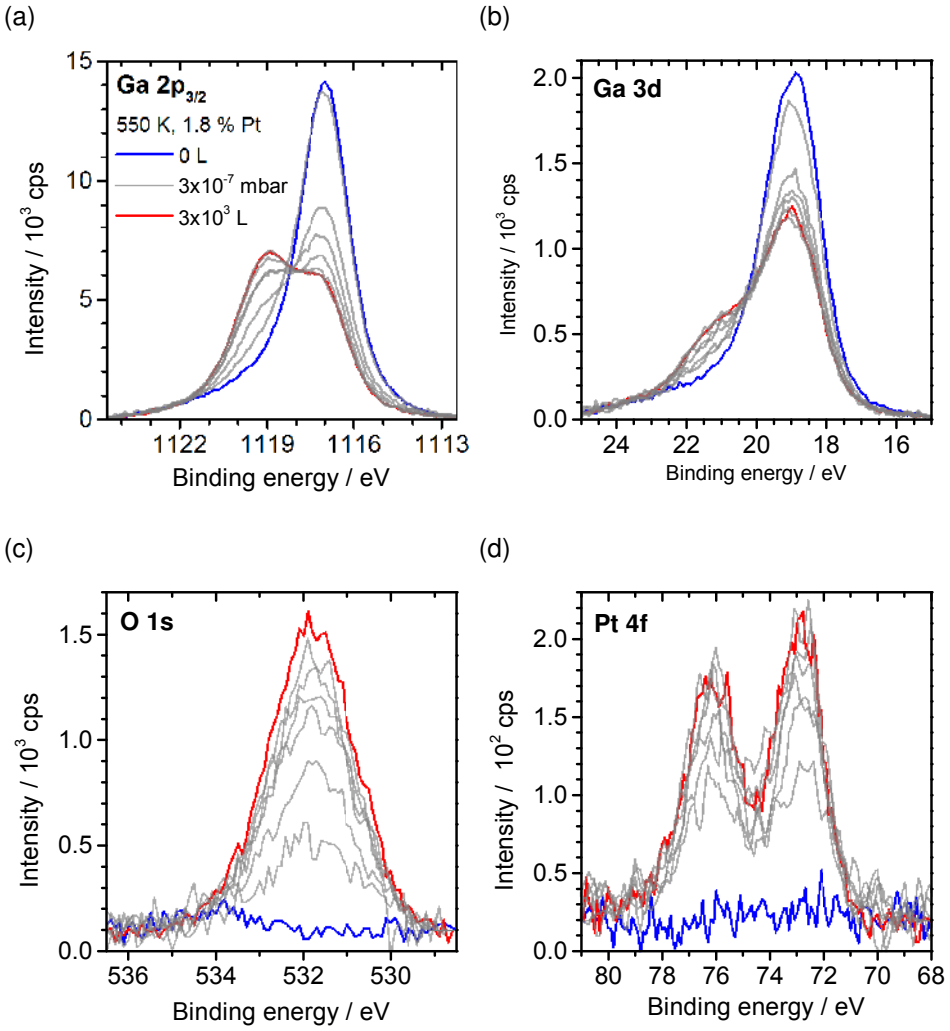

Figure 4.9.: Ga $2p_{3/2}$ (a), Ga 3d (b), O 1s (c) and Pt 4f (d) XP spectra collected from a Pt–Ga alloy with a Pt content of 1.8 at.%. The data were acquired before oxidation in UHV (blue), during oxidation at 3×10^{-7} mbar O_2 (grey) and after oxidation in UHV (red), at a sample temperature of 550 K. Oxidation was monitored for 240 min. A 3-point moving average smoothing was applied to the Pt 4f data.

and 3d regions are in good agreement with literature for Ga_2O_3.[122–124] Due to the large difference in binding energy of the Ga 2p and Ga 3d electrons, there is a large difference in kinetic energy and consequently in IMFP of the photoelectrons for these two transitions. As a result, the ID in the Ga 2p region is 37 % of the ID in the Ga 3d region of the spectrum. The oxidic components show a higher relative intensity in the Ga $2p_{3/2}$ signals. It is thus concluded that the formed oxide is primarily located at the sample–gas interface. On this basis, the thickness of the grown oxide films was determined from the Ga $2p_{3/2}$ data as a function of time and temperature, for O_2 pressures up to 1 mbar from equation (2.19).

In Figure 4.10 (a), the oxide film thickness is shown as a function of O_2 dosing time for three ex-

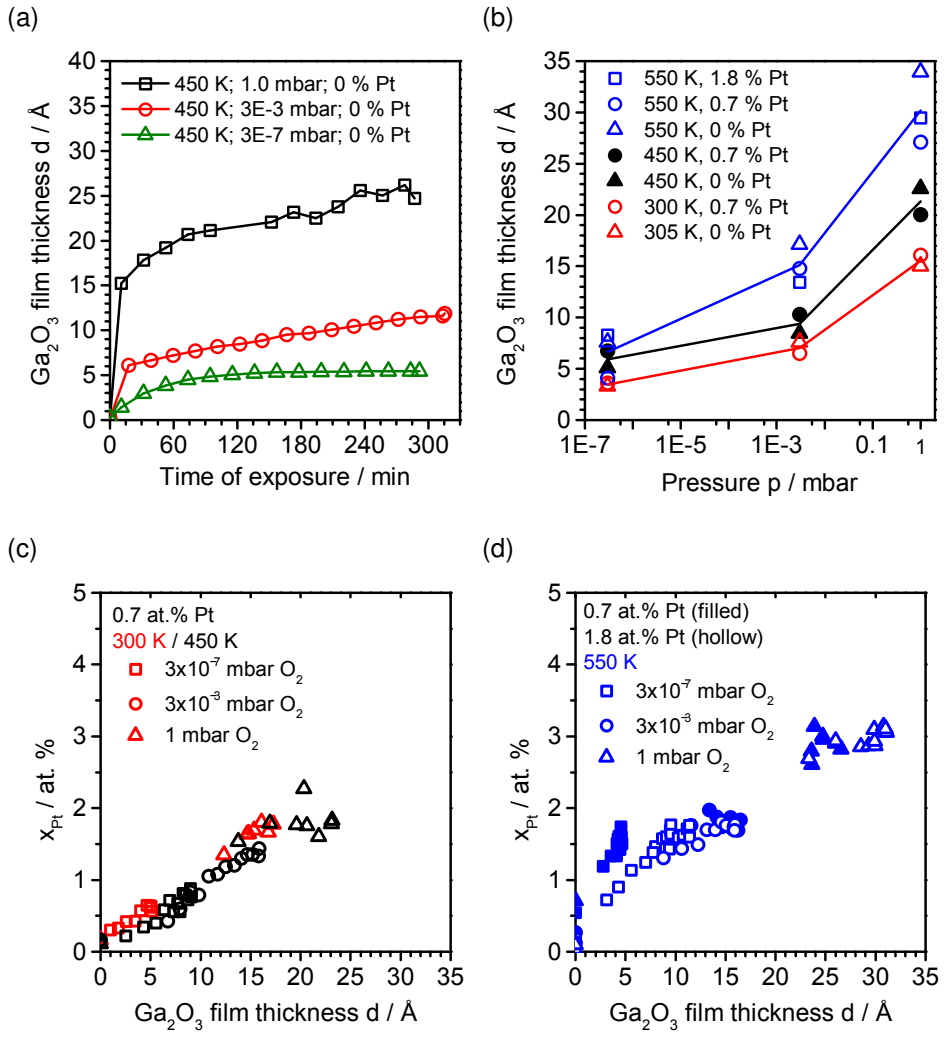

Figure 4.10.: (a) Temporal evolution of the film thickness of Ga_2O_3 on pure Ga is shown for different O_2 pressures at 450 K. (b) Ga_2O_3 thickness obtained after 120 min of oxidation for different temperatures plotted as function of pressure. (c) and (d) Pt content from quantitative analysis of Ga 3d and Pt 4f spectra plotted as function of Ga_2O_3 film thickness. For the analysis, both UHV spectra collected before and after oxidation, and *in-situ* data was used.

periments that were conducted with pure Ga at 450 K, and at three different pressures of 3×10^{-7}, 3×10^{-3} and 1 mbar (green, red, and black symbols). At 3×10^{-7} mbar O_2, the oxide thickness levels off at around 150 minutes, leading to a 5.4 Å thick oxide film. The observed saturation might be related to a strongly decreased probability for the dissociative adsorption of oxygen on the formed oxide, leading to no further increase of the apparent thickness within the time frame of the experiment.[125] At pressures of 3×10^{-3} and 1 mbar, a rapid initial increase is followed by a much slower and almost linear increase with time, which does not saturate even after 280 min. This behaviour is attributed to the growth of an oxide film, which is limited by mass transport. In a simplified picture, the kinetics would be given as $\mathrm{d}d/\mathrm{d}t \propto d^{-1}$, with the thickness d being $d \propto \sqrt{t}$ [126, 127], as qualitatively observed for 3×10^{-3} and 1 mbar oxygen pressure. We therefore ascribe the observed growth behaviour under these conditions to a diffusion-limited formation of a bulk-like oxide, which occurs after the rapid formation of a 2D surface oxide-like film structure. For the Pt-Ga alloys, the oxide growth shows a similar behavior. At 3×10^{-7} mbar O_2 the thickness after 120 min, shown in Figure 4.10 (b) scatters around a mean value of 5.5$\pm$2.2 Å. Values after saturation are 6.7$\pm$2.2 Å, in line with references [125, 128].

Because no saturation was found in the case of oxide formation at O_2 pressures of 3×10^{-3} and 1 mbar, we compare the oxide thicknesses obtained after 120 min for the samples with different Pt content. For the Ga sample and for the Pt-Ga alloys, the thickness of the grown oxide film systematically increases with pressure and sample temperature in all conducted experiments, which is shown in Figure 4.10 (b). The comparison of the samples with different Pt content, 0, 0.7 and 1.8 at.%, shows no systematic correlation between oxide film thickness and the nominal Pt content of the examined alloys. The average thicknesses of the oxide films after exposure to oxygen at 1 mbar are 16 Å at 300 K, 21 Å at 400 K and 30 Å at 550 K. Averaged values of thicknesses are also given as lines to guide the eye.

For the non-oxidized samples at temperatures below 650 K the Pt content is only 0.2 at.%, which is in contrast to the nominal bulk content of 0.7 and 1.8 at.% Pt. This is attributed to the presence of a solid Ga_6Pt phase at the examined temperatures, which is not expected according to published phase diagrams [74, 75] and has been elaborated on in more detail in the preceding Section 4.2.

During Ga_2O_3 growth, the Pt 4f intensity increases strongly, as evident from Figure 4.9 (d), shown for the sample with a nominal Pt content of 1.8 at.%. In Figure 4.10 (c) and Figure 4.10 (d), the measured Pt surface concentration is shown for all oxidation experiments conducted with the Pt-Ga alloys. The reaction temperature in these plots is color-coded, and the pressure is coded by symbols. When data obtained in UHV after oxidation is evaluated, as done for publication P1, the Pt content is found to increase linearly with increasing Ga_2O_3 thickness for all examined temperatures, indicating the incorporation of Pt atoms, or Pt-rich phases into the formed oxide film. Clearly, a linear increase in the Pt content determined from Pt 4f and Ga 3d signals with increasing Ga_2O_3 thickness is also evident at temperatures of 300 and 450 K shown in Figure 4.10 (c). Data collected in situ during the oxidation at 550 K, shown in Figure 4.10 (d), reveals further interesting aspects of the observed phenomenon. The behavior is slightly different compared to lower temperatures, as more pronounced increase in Pt content is apparent during initial growth of the oxide

film before linearly increasing Pt content is observed for higher film thickness. In agreement with the proposed Pt incorporation, the Pt content relative to Ga in Ga_2O_3 after oxidation is found to be 3.6 ± 0.6 at.% in all samples, and is independent of the film thickness and of the nominal bulk composition of the metallic alloy in the studied cases. A quantification using measured reference intensities instead of Wagners atomic sensitivity factors [129] yields a slightly higher Pt content of the Ga_2O_3 film of 5.5 ± 1.5 at.%. This behavior might be attributed to either specific structural motives containing Pt being formed during the growth of the oxide layer, or a certain solubility of Pt atoms in the formed oxide film.

The binding energy of the Pt $4f_{7/2}$ peak in the liquid alloy samples before oxidation is 72.4 ± 0.3 eV, that is shifted by +0.9 eV with respect to the value of 71.5 eV determined for the Pt(111) reference. Upon gallium oxide formation, the Pt 4f peaks further shift to higher binding energies by up to +0.9 eV, that is, by up to +1.8 eV as compared to Pt(111). This shift is to be compared with a shift of +0.7 eV upon oxygen chemisorption on Pt(110), +0.8 eV upon formation of a surface oxide on Pt(111)[130, 131], +1.1 to 1.3 eV for PtO, and +2.9 eV for Pt_2O_4.[132–136] Because the value of +1.8 eV does not agree with any of those shifts and, more importantly, due to the known thermal instability of Pt oxides under UHV and near ambient conditions [132, 137], we rule out the formation of a stable Pt oxide phase, but ascribe the observed shift to the local chemical environment of Pt atoms when incorporated into an oxygen-rich Ga_2O_3 matrix.

The observed enrichment of Pt in the oxide film at the interface might play a crucial role in understanding catalytic reactivity in reactions of similar alloy or bimetallic catalysts, particularly for reactions under oxidative conditions. The aforementioned regeneration of the catalyst by coke-burning might be facilitated by the availability of potentially active Pt species within the Ga_2O_3 film.

4.3.2. Oxidation of Pd-Ga

In analogy to the experiments conducted with the Pt-Ga alloys, Pd-Ga alloys of 0.7, 1.3 and 1.8 at.% were exposed to molecular oxygen at pressures of 3×10^{-7}, 3×10^{-5}, 3×10^{-3} and 1 mbar and a temperature of 550 K. As in case of the Pt-Ga alloy, the formation of Ga_2O_3 is observed, as deduced from the appearance of additional features in Ga $2p_{3/2}$, Ga 3d and O 1s spectra, shown in Figure 4.11 (a) to (c).

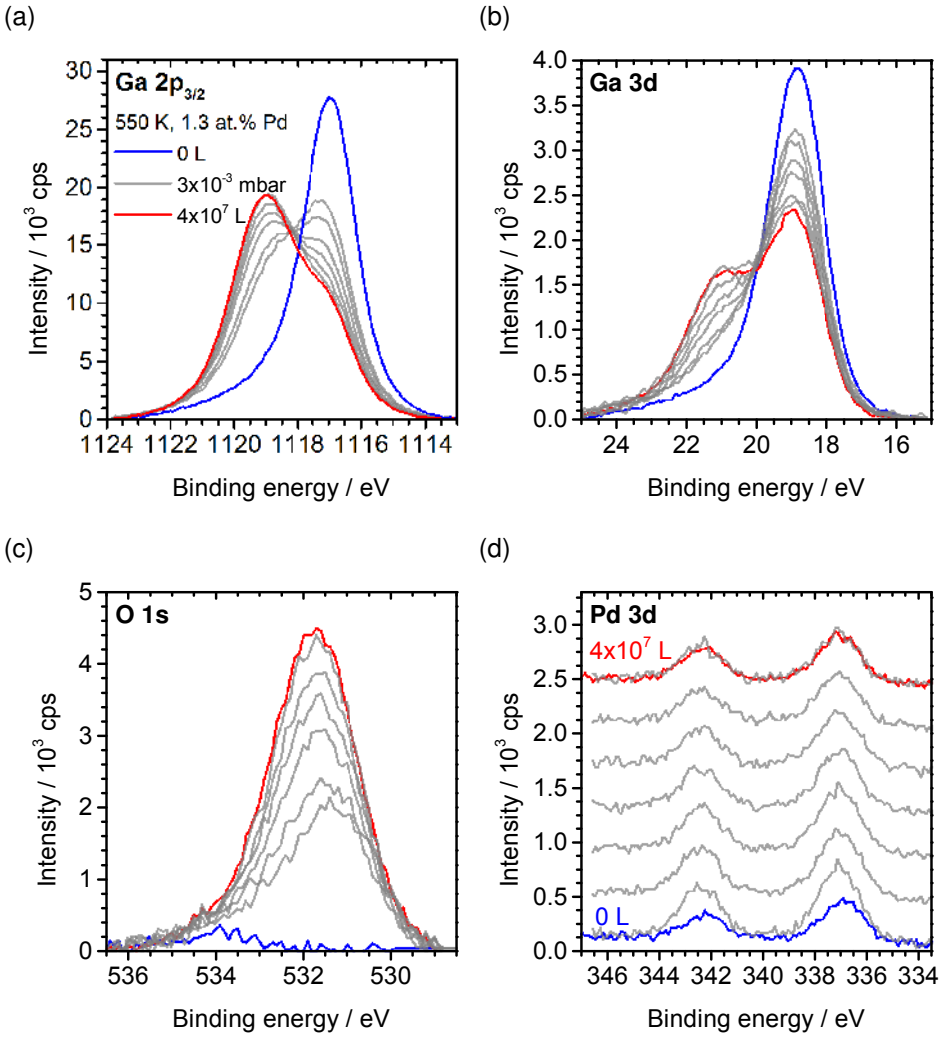

Figure 4.11.: Ga $2p_{3/2}$ (a), Ga 3d (b), O 1s (c) and Pd 3d spectra (d) collected before, after and during oxidation at a pressure of 3×10^{-3} mbar at 550 K. The nominal Pd content in the shown experiment was 1.3 at.% Pd.

Observed shifts of +2.0 eV correspond to shifts observed in the oxidation of pure Ga and Pt-Ga alloys, and a stoichiometry of $Ga_2O_{2.8\pm0.3}$ is determined from quantitative analysis of Ga 3d and O 1s signals. Growth characteristics at the different pressures are found to agree with observations for pure Ga and the Pt-Ga alloys. Film thickness is determined from Ga 3d signals using equation 2.19, as it exceeds the ID of Ga 2p signals in Ga_2O_3 for pressures of 3×10^{-3}

and 1 mbar. Contrary to the observations made for the Pt-Ga alloys, however, is the behaviour deduced from the Pd 3d spectra, shown in Figure 4.11 (d). In the first spectrum collected after exposing the sample to O_2 an increase in intensity is observed. A steady decrease in intensity is observed for spectra collected afterwards.

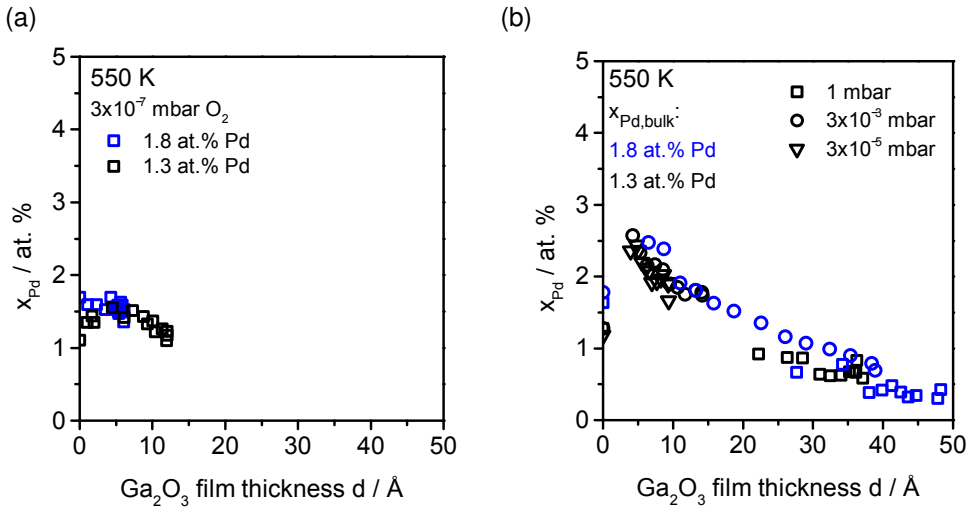

Figure 4.12.: Pd content determined from quantitative analysis of Ga 3d and Pd 3d core level signals plotted as function of the Ga_2O_3 film thickness. Shown is data collected in UHV and in-situ at 3×10^{-7} mbar (a) and at 3×10^{-5} to 1 mbar (b).

Quantitative analysis, in form of the Pd content determined from Pd 3d and Ga 3d signals as function of Ga_2O_3 film thickness is plotted in Figure 4.12 (a) for a pressure of 3×10^{-7} mbar and in Figure 4.12 (b) for pressures of 3×10^{-5}, 3×10^{-3} and 1 mbar. Aside the Pd content before oxidation, which is found to be 1.2 ± 0.1 and 1.7 ± 0.1 at.% and agrees to the nominal values of 1.3 and 1.8 at.% within the experimental uncertainty, the observed behavior during oxidation is independent of the nominal content. Temperature-dependent concentrations in the liquid, metallic alloys have been elaborated on in Section 4.2. Upon oxidation, different response to Ga_2O_3 formation is observed for the examined pressures. At 3×10^{-7} mbar only a minor increase in Pd content is observed until a thickness of 5 Å is reached. Upon further oxidation the thickness increases to up to 12 Å, while the Pd content is found to decrease again. For pressures of 3×10^{-5} to 1 mbar, an increase in Pd content by a factor of up to 2 is observed as response to initial oxide formation. At thickness exceeding 5 Å, however, similar to oxidation at 3×10^{-7} mbar the Pd content is found to steadily decrease with increasing oxide film thickness. Also the mixture of 0.7 at.% Pd shows the discussed, pressure-dependent behavior (data not shown). Quantitative analysis of Ga 3d components ascribed to Ga_2O_3 and metallic Ga, and the Pd 3d signals reveals a simultaneous decrease of the metallic Ga 3d component and the Pd 3d signals. This observation is ascribed to the similar attenuation of the two signals by the growing oxide overlayer. It is thus concluded that as response to initial formation of Ga_2O_3, an enrichment of Pd at the newly formed oxide-metal interface occurs. Contrary to Pt, however, Pd is not incorporated into the formed oxide

film, but remains enriched at the interface during Ga_2O_3 growth.

A fundamental difference between the two bimetallic systems discussed so far is the content of the transition metal in the liquid phase at the beginning of the oxidation experiments. As discussed in the preceding Sections 4.2.1 and 4.2.2, for the Pd-Ga alloys at 550 K most of the Pd is expected to be dissolved in the liquid phase. Accordingly quantitative analysis before oxidation is in agreement with the nominal bulk composition determined from weight-in. Contrary, for the Pt-Ga alloys, even at 550 K most of the transition metal will be captured in solid IMC phases, hence the low nominal Pt concentration determined from quantitative analysis before oxidation. A direct comparison of the conducted experiments has thus to be done with care. Interestingly, however, the observations made upon oxidation of the alloys behave inverse to the composition at the beginning of the experiments: While the transition metal-depleted liquid phase of the Pt-Ga system reacts by Pt incorporation and enrichment of Pt in the Ga_2O_3 film, the Pd-rich liquid phase of the Pd-Ga system reacts conversely leading to a net Pd depletion of the formed Ga_2O_3 film. As discussed, this behavior may provide evidence for a stabilization of Pt within the Ga_2O_3 film. A comparative study on the stabilization of atomically disperse Pt, and Pd in Ce_2O_3 was reported by Neitzel et al.[138] Theoretical adsorption energies of the oxygen-coordinated Pt^{2+} and Pd^{2+} ions are reported to be –678 and –504 $kJ\,mol^{-1}$. Certainly, these energies must be different for Ga_2O_3 as matrix for the transition metal ions, however, the experiments discussed above provide indication that a similar trend might be revealed for the transition metal ions in Ga_2O_3.

4.4. Deposition of Ga on gold surfaces

As for the Ga-based bimetallics discussed in preceding sections, also for Pd-Au alloy catalysts synergistic effects have been reported, e.g. in hydrodesulfurization reactions[139], low-temperature CO oxidation[140], or acetoxylation of ethylene[141]. Both Ga and Au play the role of inactive matrix or promoter in the examples discussed above. Additionally, highly disperse Au itself is known to be catalytically active since more than three decades.[142–148] Excellent review papers summarize the numerous studies reporting catalytic activity of disperse Au in different reactions, including hydrogenation of alkenes and aldehydes, dehydrogenation, CO oxidation, water gas shift, and selective oxidation.[142, 143, 145, 148] Other reviews cover the surface chemistry of various combinations of test reaction and model catalyst, ranging from the Au(111) single crystals to Au particles with sub-monolayer coverage on oxidic supports like TiO_2, MgO or FeO.[144, 145] The combination of the elements Ga and Au that will be addressed in the following, could allow for expanding the concept of catalytically active Au particles, clusters and atoms towards catalytically active single Au atoms dissolved in an inert, liquid Ga matrix, similar to what has been discussed in preceding sections and has been reported for Pd/Au[149] and Pt/Cu[150, 151].

To study the interaction of Au with Ga, an increasing amount of Ga was deposited onto polycrystalline Au foil in steps. Upon Ga deposition, the formation of a Au_7Ga_3 alloy phase with an average Ga content of 28 at.% which covers the pristine Au substrate is observed. Upon exposure of the formed Au_7Ga_3 alloy to molecular oxygen at pressures up to 1 mbar and temperatures up to 550 K, Ga within the surface-near region is oxidized to form a Ga_2O_3 phase covering the Au_7Ga_3/Au (poly) surface. For acquisition of the data shown in this Section, Mg K_α radiation was used. A schematic representation of the conducted experiments is shown in Figure 4.13.

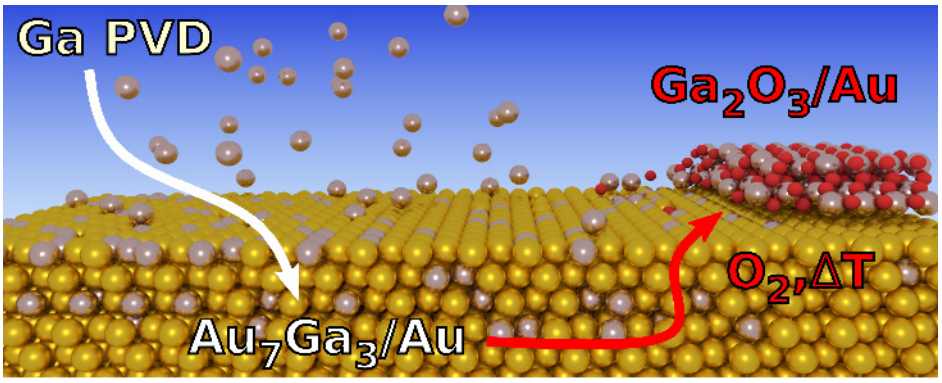

Figure 4.13.: Artists view on Au_7Ga_3 alloy formation and oxidative dealloying leading to Ga_2O_3 formation on top of the Au substrate. The shown figure was used as graphical abstract in article P5

4.4.1. Ga on polycrystalline Au surfaces – P4

A total of 19.9 Å of Ga was deposited in stepwise manner onto polycrystalline Au surfaces at sample temperatures between 300 and 330 K. Ga and Au core level signals were measured after each deposition step. The Ga $2p_{3/2}$ and Ga 3d signals (Figure 4.14 (a)) are found to increase until saturation. Simultaneously, the Au $4f_{5/2}$ and $4f_{7/2}$ substrate signals (Figure 4.14 (b)) are attenuated to about 70 % of their initial intensity.

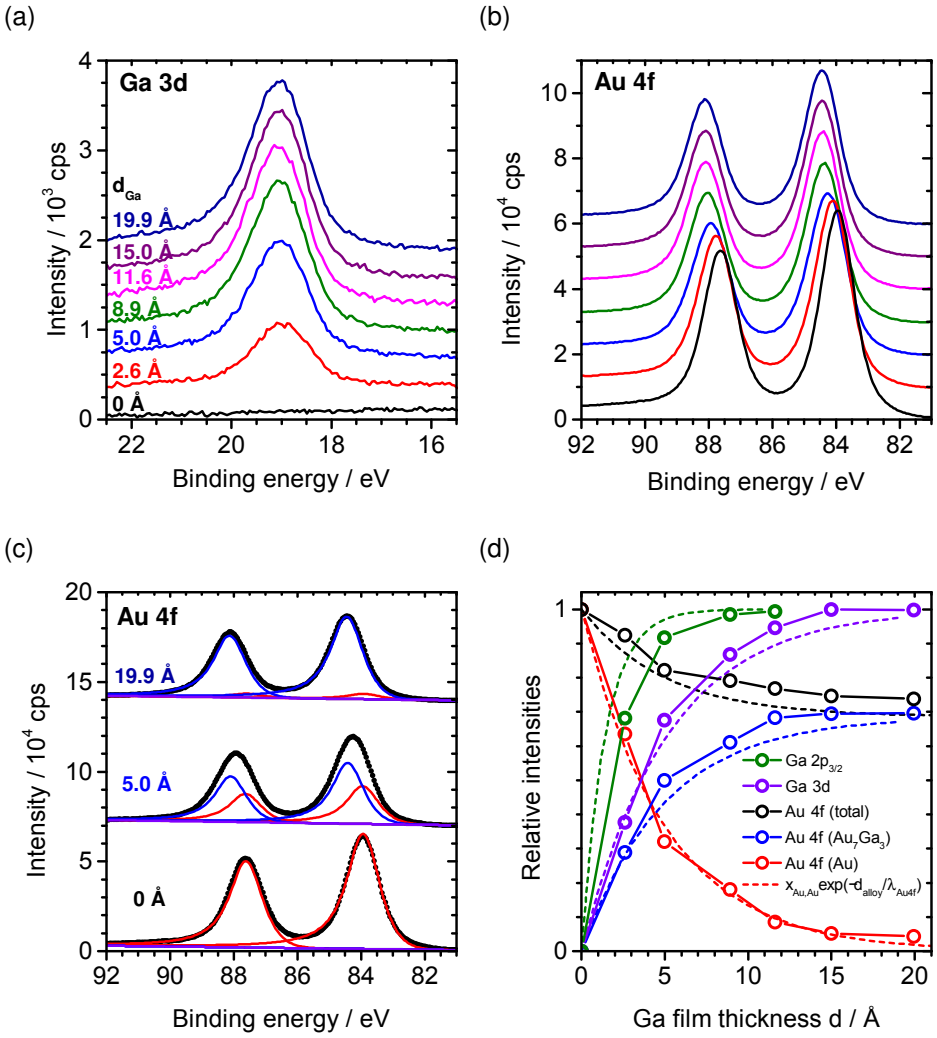

Figure 4.14.: (a) Ga 3d, and (b) Au 4f XP spectra, collected during stepwise deposition of Ga on a Au foil. (c) Peak fitting of Au 4f peaks with two components, assigned to the Au substrate (red) and the Au_7Ga_3 alloy (blue), for selected thicknesses. (d) Relative intensities of Au 4f, Ga $2p_{3/2}$ and Ga 3d signals plotted as function of the nominal Ga thickness, along with the calculated attenuation of Au 4f substrate signals expected for continuous growth of a Au_7Ga_3 overlayer (dashed red line). Calculated intensities of the other signals are shown as dashed lines colored according to the color code used for data points.

The binding energies of the Ga $2p_{3/2}$ signal at 1117.1 eV and Ga 3d signal at 19.1 eV are independent of the amount of Ga deposited, and are in reasonable agreement with values discussed for metallic Ga in preceding sections. In contrast, the Au $4f_{7/2}$ peak shows a pronounced shift to higher binding energy from 83.9 to 84.4 eV, which is due to the evolution of a new component shifted by 0.5 eV relative to the pristine substrate. This is ascribed to the formation of a Ga-Au alloy phase. The Au 4f spectra were therfore fitted with two components representing the unchanged Au substrate and the newly formed alloy (denoted as Au_7Ga_3 – see below). Fitted Au 4f spectra of the clean Au surface and the second and last Ga deposition steps are shown in Figure 4.14 (c). The difference in binding energy is attributed to the Ga-Au interaction; From valence band spectra, possible work-function changes of the detector as origin of this shift are ruled out. Au 4f binding energy shifts of similar magnitude were reported in literature for liquid alloy phases (T > 723 K) [152]. An effect similar to the increased occupancy of Pd 4d states, resulting in better Pd 3d hole state shielding and decreased final state screening, which was discussed for the Pd-Ga system before, might also be responsible for the shifts observed in the Ga-Au system. The proposed formation of a Ga-Au alloy phase is also supported by the quantitative analysis of the XP spectra as function of the nominal thickness of deposited Ga, which is shown in Figure 4.14 (d). The Au signals are normalized to the initial value of the clean Au surface, and the Ga signals to the intensity at saturation. A constant Ga content of 28$\pm$3 at.% during and after the deposition is determined from quantitative analysis of the Au 4f alloy component and Ga 3d signals. Quantitative analysis was done according to equation (2.15). When using the tabulated photoionization cross sections reported by Yeh[99] a slightly larger value of 29 ± 3 at.% is found. Considering an estimated uncertainty of $\pm$10 % the determined composition is in good agreement with values of a homogeneity range of 29.8 to 31 at.% reported for the γ and γ' Au_7Ga_3 IMC [153, 154]. Therefore, the formed alloy phase is identified as Au_7Ga_3, and this assignment is used in text and figures, although the presence of mixtures of different IMCs or random alloys with the same average stoichiometry cannot be ruled out. For the Ga $2p_{3/2}$ signal (green data points in Figure 4.14 (d)), the quantitative analysis reveals that saturation of the peak intensity is quickly reached within the first three deposition steps, equivalent to approx. 9 Å Ga. For the Ga 3d signal intensity (purple data points), saturation is reached only above a nominal Ga film thickness of 15 Å. For a pure Ga deposit, the Ga $2p_{3/2}$ and Ga 3d signals should saturate during deposition only at Ga thicknesses exceeding the information depth of the Ga signals in pure Ga (i.e. 19 and 81 Å). In the experiment, however, the saturation of the Ga signals occurs at much lower nominal thickness for both Ga $2p_{3/2}$ and Ga 3d at 9 and 15 Å. In particular the thickness of 9 Å determined from the saturation of the Ga $2p_{3/2}$ signal is closer to the value expected for Ga in a Au matrix with an information depth of 12 Å than to the value expected for pure Ga of 18.8 Å. This behavior therefor strongly indicates the formation of a Au-rich bimetallic Ga-Au phase, in agreement to quantitative analysis. In accordance to the proposed formation of Au_7Ga_3 layers on top of the substrate, the relative intensity of the Au 4f substrate component at 83.9 eV agrees with the calculated attenuation by a continuously growing Au_7Ga_3 film. An exponential fit to the experimental data was used to calibrate our Ga deposition rate. The Au 4f intensity calculated according to $I/I_0 = e^{-d/\lambda_{Au\ 4f,Ga_3Au_7}}$ is

shown as a dashed red line in Figure 4.14 (d), while calculated intensities for the alloy-related core level signals are shown as dashed lines, colored according to the experimental data. They agree with the data within the experimental uncertainty. For the IMFP calculation, and the calculation of the Au_7Ga_3 thickness from the amount (that is, the nominal thickness) of deposited Ga, the alloy phase is treated as random alloy of Ga in Au; the materials constants are estimated according to SI Equations S6 to S8 and Table S1 ((Au $4f_{7/2}$) = 16.0 Å, d(Au_7Ga_3) = 3.24 x d(Ga)) in the supplemental information of publication P5.

To investigate the reactivity of this Au_7Ga_3 alloy, it was exposed to 3×10^{-7}, 3×10^{-3}, 0.3 and 1 mbar of molecular oxygen for 210, 150, 150 and 150 min at room temperature. The corresponding Au 4f and Ga 3d spectra measured in-situ after oxygen saturation was reached are shown in Figure 4.15 (a) and Figure 4.15 (b), respectively (green curves). In addition, the spectra of the clean Au surface (black), the Au_7Ga_3 alloy (red), and the alloy after oxidation at 1 mbar at 550 K (for 30 min), all collected in UHV, are shown. The absolute intensities at 0.3 and 1.0 mbar are influenced by attenuation of the photoemission signals by the gas phase between surface and detector.

The Ga 3d spectra in Figure 4.15 (b) show significant changes starting at O_2 pressures of 3×10^{-3} mbar. At 0.3 and 1 mbar O_2, an additional feature at 20.4 eV is clearly visible, which is shifted by + 1.3 eV to higher binding energy with respect to the signal of the alloy at 19.1 eV. In combination with an emerging O 1s peak at 531.3 eV, this clearly indicates a partial oxidation of Ga within the detection range of XPS. This oxidation goes along with a strong increase in Ga signal intensities and a decrease in the Au 4f intensity. An additional shift by 0.2 eV, as well as further increase in the Ga 3d and decrease in the Au 4f signal intensity is observed after exposure to 1 mbar O_2 at an elevated temperature of 550 K. The Ga_xO_y formation goes along with a shift of the Au 4f signals to lower binding energy – reversing the shift observed during deposition. This behavior is also evident from the quantitative analysis in Figure 4.15 (c), where the different Ga (reduced and oxidized) and Au (Au_7Ga_3 and Au) signals are plotted as function of the oxygen pressure. The alloy-related Au 4f component is found to decrease in intensity with increasing degree of Ga oxidation. The observed behavior indicates that upon exposure to oxygen the Au_7Ga_3 phase vanishes in favor of the Ga oxide formed on top. This also is in line with the increase in Ga 3d and decrease in Au 4f signal intensity, which is explained by increased attenuation of Au signals by the formed Ga_xO_y. Compared to the Au_7Ga_3 phase, the Ga_xO_y layer has a higher Ga atom density, which explains the increase in Ga 3d intensity if formed on top of the alloy surface. In the Ga $2p_{3/2}$ spectra Ga_2O_3-related features for the different oxidation steps are generally found to be more pronounced than in the Ga 3d spectra, indicating Ga_2O_3 film formation at the alloy-vacuum interface. From the quantitative analysis of Ga 3d and O 1s spectra, we deduce a stoichiometry of $Ga_2O_{2.7}$. The maximum shifts in the Ga $2p_{3/2}$ and Ga 3d signals at 1118.6 and 20.6 eV amount to 1.5 eV relative to the metallic alloy, and 2.1/2.3 eV relative to values of 18.5[124]/18.3 eV[122] reported for the Ga 3d signal of pure Ga (2.2 eV shift, relative to 1116.4 eV[122] for the Ga $2p_{3/2}$ signal). These shifts are in good agreement with shifts of 2.1 (Ga 3d) and 2.4 eV (Ga 3d, Ga $2p_{3/2}$) reported for bulk Ga_2O_3. From the attenuation of the Au 4f

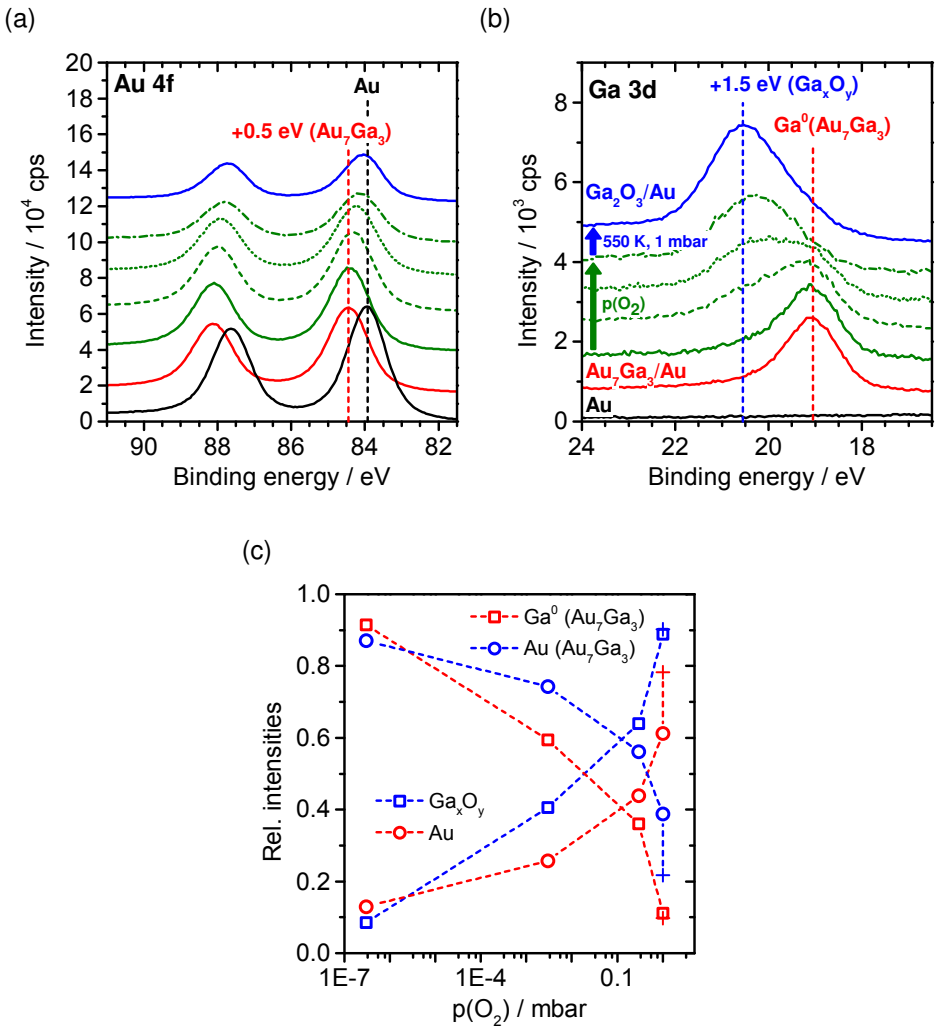

Figure 4.15.: (a) Au 4f and (b) Ga 3d spectra, of the clean surface in UHV (black), after the formation of the Au_7Ga_3 alloy in UHV (red), in situ during exposure of the alloy to 3×10^{-7}, 3×10^{-3}, 0.3 and 1 mbar O_2 at room temperature (green), and after exposure to 1 mbar at 550 K (blue) measured in UHV. Please note that Ga 3d signals (and the O 1s signals – see SI) collected at 1 mbar are shifted by +0.3 eV to align to the O 1s peaks of the oxide. (c) Relative intensities of metallic and oxidized Ga components, and Au 4f components of the alloy and substrate. Crosses indicate the measurement in UHV after exposure to 1 mbar O_2 at 550 K.

signals, the thickness of the Ga_xO_y film is estimated to be 18.7 Å, which equals a 14.0 Å thick pure solid Ga film with respect to the Ga atom density. The same estimate for the alloy with 28 at.% Ga in Au yields a value of 15.5 Å, which is in reasonable agreement. In agreement with the quantitative analysis of Au 4f signals, these numbers indicate a pronounced dealloying of the surface-near alloy upon Ga oxidation and rapid Ga/Au/O diffusion. The difference with respect to the total deposited amount of Ga, that is 19.9 Å, is attributed to incomplete dealloying and loss of Ga by diffusion into the Au bulk.

5. Summary

A novel class of catalyst materials, namely alumina/silica-supported Ga-rich bimetallic Pd-Ga and Rh-Ga phases, active in the dehydrogenation of alkanes, as well as liquid or biphasic model systems for the former were examined using a combination of XPS, in-situ NAP-XPS and temperature-dependent ARXPS measurements.

The supported bimetallic catalysts, prepared and subjected to catalytic testing by Dr. N. Taccardi and J. Debuschewitz from the work group of Prof. Dr. P. Wasserscheid, demonstrated remarkable stability in the challenging catalytic dehydrogenation of butane. Common Pt catalysts are prone to deactivation by coke formation, due to high temperatures needed to achieve reasonable yields, and industrial processes therefore include frequent catalyst regeneration.

The novel bimetallic catalysts, however, are able to maintain constant activity for remarkable times of up to 100 h. Specific activities determined in catalytic testing were comparable, or did even exceed the activity of the pure transition metal catalysts by an order of magnitude. The same holds for the selectivity towards the corresponding reaction product butene. Catalysts of low transition metal contents, that is, concentrations as low as 2 at.% (Pd) and 1 at.% (Rh), are found to be particularly well-performing. This astonishing behavior is ascribed to the presence of Ga-rich phases. These are assumed to be the active catalyst phase, and due to their high Ga content, they are in the liquid state under reaction conditions, which is held responsible for their stability and resilience to coke formation. To shed light on the reasons and mechanisms behind these observations, a number of experiments were conducted within this thesis.

First, the characterization of SiO_2/Al_2O_3-supported Pd-Ga and Rh-Ga catalysts was done using XPS. The loadings determined from quantitative analysis of XPS data, 13 ± 1 and 1.5 ± 0.5 wt.% Ga, and Pd respectively, are found to exceed the nominal loading of 4.9 wt.% Ga and 0.4 wt.% Pd in the examined Pd-Ga samples. This is expected for such analysis, which due to the limited information depth of the method, will overestimate the catalyst loading. The Pd content of 6.7 at.% with respect to Ga, on the other hand, is found to be in reasonable agreement with the nominal value of 4.5 at.%. For the Rh-Ga system, samples of different nominal compositions but constant Ga loading of 5.8 ± 0.3 wt.% were examined after preparation, and after catalytic testing. XPS analysis of the data collected from as-prepared samples showed an invariant Rh concentration of 25 ± 6 at.% with respect to Ga, despite the nominal ratios varying from 5.8 to 1.1 at.%. This indicates a high surface affinity of Rh in the examined systems. Accordingly, the loadings of 18 ± 4 and 6 ± 1 wt.% Ga, and Rh respectively, are found to only slightly differ in the examined samples. Due to sample preparation and transfer in air, most of the Ga and all of the Rh probed by the surface sensitive XPS measurement is oxidized after preparation. The analysis, however, revealed the presence of reduced Ga and Rh species after catalytic testing despite the transfer

in air. This is deduced from spectroscopic features in the Ga 3d and Rh $3d_{5/2}$ spectra, which are shifted to lower binding energy by 2.0 eV with respect to the values observed in the as-prepared samples. These features are found to be strongly increased after catalytic testing, which indicates the formation of either pure Rh or Ga phases, or the formation of alloy or intermetallic compounds under reaction conditions consuming oxidized Ga and Rh species.

Beside the powder catalyst samples, also model systems for the former were examined. Three different transition metals, Rh, Pt and Pd were combined with Ga to produce bimetallic alloy materials with transition metal contents typically below 2 at.%. These were examined in a temperature range from room temperature to 850 K using angle-resolved XPS measurements. For all three examined systems, phase-separation into transition metal-rich intermetallic compounds and a liquid phase is observed within the probed temperature and composition range. Variation of the sample temperature leads to systematic variation of the composition of the liquid phase by precipitation or melting of the transition metal-rich intermetallic phases. These observations are in qualitative agreement with published bulk phase diagrams. Furthermore, a surface depletion of the transition metals is deduced from quantitative analysis or relative core level intensities collected in angle-resolved XPS measurements. The liquidus temperature determined from the analysis for mixtures of comparable stoichiometry, as well as the extent of surface depletion of the transition metal atoms decreases in the order Rh > Pt > Pd, which is in line with thermodynamic data. For the Pd-Ga system, the spectroscopic data was quantitatively compared to results of a DFT-based MD simulation by J. Erhard in the workgroup of Prof. Dr. A. Görling. By modeling XPS intensities of a structured system, the Pd surface depletion and Pd enrichment in the second, subsurface layer formed in the liquid phase by stratification, as it is observed in the MD simulation, could be corroborated. This indicates that the stability of the supported catalysts observed in catalytic testing is due to the isolation and limited concentration of active centers at the liquid–gas interface, and suggests a mechanism that involves the emergence of active centers from the bulk to the interface.

Furthermore, the growth of Ga_2O_3 films on pure liquid Ga as well as the growth on the liquid phases of Pt-Ga and Pd-Ga alloys of nominal transition metal contents below 2 at.% was examined in situ using NAP-XPS. Samples were exposed to molecular oxygen at pressures of 3×10^{-7} to 1 mbar, at temperatures between room temperature and 550 K. Different growth modes of the wetting oxide films were observed as function of pressure, and the temperature- and pressure-dependence of the thickness was derived. For 3×10^{-7} mbar, film thicknesses were found to be asymptotically approaching an average value of 7 ± 2 Å. This is ascribed to the limitation of lateral, two-dimensional growth by the availability of metallic Ga. The latter leads to asymptotic increase of the oxide-covered surface area, and thus to asymptotic increase of the apparent film thickness determined from the area-integrating XPS measurements. At the elevated pressures of up to 1 mbar, after a rapid initial oxidation, due to two-dimensional growth enhanced by the increased pressure, linear growth of the oxide thickness is observed. In the conducted experiments, films of up to 37 Å were examined, and their thickness is shown to increase with temperature and pressure. Furthermore, a very fundamental difference in the response to Ga_2O_3 formation upon oxidation

is revealed for the Pt-Ga and Pd-Ga systems. Within the examined compositional range and parameter space of the experiments, the Pt-Ga system incorporates homogeneously distributed Pt into the formed oxide, while for the Pd-Ga alloys Pd-enrichment at the Ga_2O_3–Ga interface is observed, and Pd is not incorporated into the oxide film. For the Pt-Ga alloys, where the Pt content of the film is found to be 5.5±1.5 at.%, this behavior corresponds to a net enrichment of Pt at the newly formed Ga_2O_3-vacuum interface and in the oxide film. The incorporation of Pt into the Ga_2O_3 film is accompanied by a +1.8 eV shift in the Au 4f signals with respect to values observed for the Pt(111) surface, which is ascribed to Pt atoms or clusters in oxygen-rich Ga_2O_3 matrix. For the Pd-Ga alloys, the presence of minor Ga_2O_3 content corresponding to 5 Å provokes interfacial enrichment of Pd, increasing the apparent Pd surface concentration by a factor of 2. For Ga_2O_3 films up to 50 Å, however, the apparent Pd content is found to decrease with increasing thickness, which is ascribed to signal attenuation by the growing overlayer, and leads to the conclusion that Pd remains located at the metal–oxide interface. Accordingly, no shifts are observed in the Pd 3d signals during oxidation. Based on these results, the formation of thick oxide films under reaction conditions may have a deactivating effect on the supported Pd-Ga catalyst, while a minor Ga_2O_3 content may increase the number of active Pd sites at the interface. Also for the Pt-Ga system, presence of oxygen may lead to an increase in active sites at the interface.

Finally, the interaction between Ga and Au was studied by physical vapor deposition of Ga onto polycrystalline Au. This rather unconventional combination of elements provides potential to expand the concept of catalytically active single Au atoms to active Au centers submerged in a Ga matrix similar to the Pt/Pd/Rh-Ga systems examined before. In first test experiments, the formation of a continuously growing alloy film of average composition Au_7Ga_3 on top of polycrystalline Au surfaces, and the consecutive oxidative dealloying of the newly formed surface by the formation of a Ga_2O_3 overlayer at room temperature and pressures up to 1 mbar was followed by in-situ XPS. Changes in the Au 4f spectroscopic fingerprint, that is, the emergence of an additional component shifted by 0.5 eV with respect to the substrate signal, due to alloying, are shown to be reversible by the oxidative dealloying. Similarly to experiments conducted with Pd/Pt/Rh-Ga mixtures, further experiments may include liquid solutions of Au in Ga.

6. Zusammenfassung

Mittels Röntgenphotoelektronenspektroskopie (XPS) wurden Proben eines neuartigen Katalysatormaterials – namentlich geträgerte, galliumreiche Legierungen von Ga und den katalytisch aktiven Übergangsmetallen Pd und Rh – untersucht. Vergleichende Experimente wurden an Modellsystemen in Form makroskopisch großer Proben galliumreicher Legierungen mittels Hochdruck-XPS, sowie temperatur- und winkelaufgelöster XPS durchgeführt.

Die verschiedenen Proben geträgerter Katalysatoren wurden von Dr. N. Taccardi und J. Debuschewitz, Mitarbeiter der Arbeitsgruppe um Prof. Dr. P. Wasserscheid, hergestellt, und anschließend hinsichtlich ihrer katalytischen Aktivität in der Dehydrierung von Butan untersucht. Hierbei konnte gezeigt werden, dass die auf Ga basierenden Materialien, im Vergleich zu herkömlichen Pd/Pt Katalysatoren, herausragende Eigenschaften besitzen. Die Dehydrierung leichter Alkane stellt eine äußerst anspruchsvolle Reaktion dar, da, um wirtschaftliche Umsätze zu erzielen, hohe Reaktionstemperaturen benötigt werden. Mit erhöhter Reaktionstemperatur steigen allerdings auch die Raten konkurrierender Prozesse wie Isomerisierung oder die Verkokung. Herkömmliche Pt Katalysatoren leiden daher unter schneller Deaktivierung, und kommerzielle Prozesse setzen auf häufige oder kontinuierliche Regeneration durch Koksbrennen. Die neuartigen, galliumreichen Systeme hingegen zeigten sich auch nach 100 h noch nahezu unverändert aktiv. Die spezifischen Aktivitäten, und Selektivitäten der galliumreichen Katalysatoren sind teils um eine Größenordnung höher er als die der reinen Pd/Pt Katalysatoren. Die Proben mit dem kleinsten Übergangsmetallgehalt von ungefähr 2 at.% (Pd) und 1 at.% (Rh) zeigten sich hierbei besonders effizient. Die positiven Aspekte, die durch das Beimengen hoher Ga Anteile entstehen, werden dem Vorhandensein galliumreicher Phasen zugeschrieben. Diese sind, auf Grund des hohen Ga Anteils, unter Reaktionsbedingungen teilweise flüssig. Es wird vermutet, dass flüssige Phasen die katalytisch aktive Phase darstellen, die im Gegensatz zu übergangsmetallreichen, festen Phasen nicht durch schnelle Verkokung passivieren. Um Licht auf die den geschilderten Beobachtungen zu Grunde liegenden Ursachen und Mechanismen zu werfen, wurden im Rahmen der vorliegenden Arbeit eine Reihe von Experimenten durchgeführt.

Zunächst wurden Proben von SiO_2 bzw. Al_2O_3 geträgerten Pd-Ga und Rh-Ga Katalysatoren mittels XPS charakterisiert. Die aus der Analyse der XPS Daten bestimmten Beladungsgrade von 13 ± 1 wt.% Ga und 1.5 ± 0.5 wt.% Pd für die untersuchten Pd-Ga Proben weichen von den nominellen Werten (4.9 wt.% Ga, 0.4 wt.% Pd) ab. Eine quantitative Auswertung der XPS Daten zur Bestimmung der Beladung des Katalysators muss allerdings auf Grund der geringen Informationstiefe der Methode ein die nominellen Werte übersteigendes Ergebnis liefern. Der Pd Gehalt von 6.7 at.% im Verhältnis zu Ga stimmt innerhalb akzeptabler Grenzen mit dem nominellen Wert von 4.5 at.% überein. Es wurden ferner Proben des Rh-Ga Systems mit konstanter Ga Beladung

von 5.8 ± 0.3 wt.%, und variiertem Rh Gehalt zwischen 5.8 und 1.1 at.% untersucht. Hierbei zeigen die XPS Daten der Proben nach Präparation einen indentischen Rh Gehalt von 25 ± 6 at.% im Verhältnis zu Ga, was für eine besondere Affinität des Rh zur Oberfläche der untersuchten Materialien spricht. Entsprechend variieren auch die Beladungsgrade, bestimmt aus der quantitativen Analyse der XPS Daten, nur mäßig und nicht systematisch. Es werden Werte von 18 ± 4 wt.% Ga und 6 ± 1 wt.% Rh bestimmt. Da die Proben teils an Luft präpariert und transferiert wurden, liegen große Teile des spektroskopisch erfassbaren Ga und Rh in oxidierter Form vor. Die Analyse der XPS Daten von Proben, die katalytischen Tests unterzogen worden waren, zeigt allerdings, dass sich unter den Reaktionsbedingungen im Testreaktor reduzierte Ga und Rh Spezies an der Katalysatoroberfläche bilden. Spektroskopisch äußert sich dies in Form zusätzlicher Komponenten in den Ga 3d und Rh 3d Signalen, welche, relativ zu den Bindungsenergien die nach Präparation beobachtet werden, um 2.0 eV verschoben sind. Jene zusätzlichen Komponenten tauchen im Falle des Rh 3d Signals erst durch die Reaktion im Testreaktor auf, während sie im Falle des Ga 3d Signals eine Verstärkung erfahren. Für beide Elemente deutet dies auf die Bildung reiner Ga oder Rh Phasen, oder auf die Bildung von Mischphasen aus den oxidierten Spezies unter Reaktionsbedingungen hin.

Neben geträgerten Katalysatoren wurden auch passende Modellsysteme untersucht. Hierzu wurden drei unterschiedliche Übergangsmetalle, Rh, Pt, und Pd mit Ga zu bimetallischen Legierungen kombiniert. Typischerweise lag hierbei der Gehalt der Übergangsmetalle unter 2 at.%. Derartige Proben wurden dann innerhalb eines Temperaturintervalls zwischen Raumtemperatur und 850 K mittels winkelaufgelöster XPS untersucht. Für jedes der drei untersuchten Systeme wurde innerhalb des untersuchten Parameterraums eine Phasentrennung in feste, übergangsmetallreiche, intermetallische Phasen und eine flüssige Phase beobachtet. Die Variation der Probentemperatur führte, in qualitativer Übereinstimmung mit in der Literatur veröffentlichten Phasendiagrammen, zu einer Variation des Übergangsmetallgehalts der flüssigen Phase durch Bildung oder Schmelzen der intermetallischen Verbindungen. Ferner wurde, abgeleitet aus winkelaufgelösten XPS Messungen, eine Verarmung der Übergangsmetalle an der Oberfläche der flüssigen Phase beobachtet. Die Liquidustemperaturen von Mischungen vergleichbarer Zusammensetzung, sowie das Ausmaß der beobachteten Verarmung der Oberfläche nehmen Gemäß der Reihenfolge Rh > Pt > Pd ab. Im Falle des Pd-Ga Systems wurde die quantitative Analyse der XPS Daten mit den Ergebnissen von Molekulardynamiksimulationen verglichen. Die Simulationen wurden von J. Erhard aus der Arbeitsgruppe um Prof. Dr. A. Görling durchgeführt und ausgewertet. Durch den Vergleich mit den experimentellen Werten, konnte die Pd Verarmung der Grenzfläche zwischen Flüssigkeit und Vakuum, sowie eine Anreicherung in der zweiten und dritten Lage nachgewiesen werden. Diese Ergebnisse deuten darauf hin, dass die Stabilität der realen Katalysatorsysteme auf die Isolation und Verarmung potentiell katalytisch aktiver Atome in der Grenzfläche zwischen flüssiger, aktiver Phase und Vakuum zurückzuführen sein könnten.

Das Wachstum von Ga_2O_3 Filmen auf reinem, flüssigem Ga, sowie auf den flüssigen Phasen von Pt-Ga und Pd-Ga Mischungen wurde in situ mittels Hochdruck XPS untersucht. Der Übergangsmetallgehalt der Mischungen lag hierbei unter 2 at.%. Sämtliche Proben wurden bei Tem-

peraturen zwischen Raumtemperatur und 550 K molekularem Sauerstoff mit einem Gesamtdruck zwischen 3×10^{-7} und 1 mbar ausgesetzt. In Abhängigkeit des Druckes konnten verschiedene Wachstumsmodi beobachtet werden. Ferner konnte die Abhängigkeit der Schichtdicke der Oxidfilme als Funktion des Druckes und der Temperatur erfasst werden. Bei 3×10^{-7} mbar zeigte sich eine asymptotisch gegen einen Mittelwert von 7 ± 2 Å konvergierende Entwicklung der aus der XPS berechneten Schichtdicke. Das beobachtete Verhalten wird auf zweidimensionales Wachstum bei niedrigen Drücken zurückgeführt. Hierbei ergibt sich in Näherung eine der verbleibenden Fläche metallischen Galliums direkt proportionale Wachstumsrate. In Konsequenz ergibt sich daraus eine asymptotisch zunehmende durch das Oxid bedeckte Fäche, was sich im beschriebenen, asymptotischen Verlauf der aus der flächenintegrierenden XPS Messung bestimmten (scheinbaren) Schichtdicke äußert. Bei höherem Druck wurde nach einem sprunghaften Anstieg zu Begin der Oxidation, welcher primär auf die durch den erhöhten Druck beschleunigte Bildung des zweidimensional wachsenden Öberflächenoxidesßurückzuführen ist, eine lineare Zunahme der Dicke des Oxidfilms beobachtet. Es konnte die Zunahme der Schichtdicke mit steigender Temperatur und steigenden Drücken gezeigt werden; Schichtdicken bis 37 Å wurden untersucht. Die Reaktion der beiden untersuchten Systeme (Pt-Ga, und Pd-Ga) auf die Bildung der Ga_2O_3 Filme unterscheidet sich stark. Innerhalb des untersuchten Parameterraums zeigt sich, dass bei Oxidation der Pt-Ga Legierungen homogen verteiltes Pt in den wachsenden Filmen eingelagert wird. Die Menge des derart gebundenen Pt im Verhältnis zu $Ga^{\delta+}$ in Ga_2O_3 ergibt sich zu 5.5 ± 1.5 at.%, was einer Pt-Anreicherung an der Probenoberfläche und im gebildeten Oxidfilm entspricht. Dieser Einschluss von Pt Atomen oder Clustern in einer sauerstoffreichen Matrix von Ga_2O_3 geht mit einer Verschiebung der Pt 4f Signale um 1.8 eV relativ zur Bindungsenergie der Signale einer Pt(111) Oberfläche einher. Die untersuchten Pd-Ga Mischungen zeigen zwar eine Pd-Anreicherung an der neu gebildeten Metall-Oxid Grenzfläche, es wird aber kein Pd in den wachsenden Oxidfilm eingeschlossen. Die quantitative Analyse zeigt zunächst eine Erhöhung der Pd Oberflächenkonzentration um etwa einen Faktor 2 als Reaktion auf die Bildung geringer Mengen Ga_2O_3 (entsprechend einer Schichtdicke von bis zu 5 Å). Für dickere Filme nimmt die scheinbare Oberflächenkonzentration des Pd mit zunehmender Schichtdicke ab, was mit der Dämpfung der zur quantitativen Analyse herangezogenen Pd 3d Signale durch die aufwachsende Ga_2O_3 Schicht erklärt wird. Es zeigt sich hierbei erwartungsgemäß keine Verschiebung der Bindungsenergie der Pd 3d Signale. Die gezeigten Ergebnisse lassen den Rückschluss zu, dass die Bildung dicker Ga_2O_3 Filme unter Reaktionsbedingungen eine passivierende Wirkung auf die geträgerten Pd-Ga Katalysatoren haben könnte. Die Bildung geringer Mengen des Oxids könnte die Anzahl aktiver Zentren an der Katalysatoroberfläche allerdings erhöhen. Gleichermaßen könnte die Oxidation der geträgerten Pt-Ga Katalysatoren die Anzahl aktiver Zentren an der Katalysatoroberfläche erhöhen, und damit Einfluss auf die Effizienz der Reaktion nehmen.

Zuletzt wurde die Wechselwirkung zwischen Gallium und Gold mittels XPS und der schrittweisen Gasphasenabscheidung von Gallium auf polykristallinen Goldfolien untersucht. Diese für die heterogene Katalyse eher ungewöhnliche Kombination von Elementen bietet die Möglichkeit, in Anlehnung an die diskutierten Pt/Pd/Rh-Ga Systeme, die Konzepte um katalytisch aktives, di-

sperses Gold auf aktive Goldatome in einer Matrix flüssigen Galliums zu erweitern. In ersten Testexperimenten konnte die Bildung einer kontinuierlich wachsenden Schicht einer Legierung mit der Zusammensetzung Au_7Ga_3 verfolgt werden. Mittels Hochdruck-XPS konnte anschließend die Oxidation des in der Legierung gebundenen Galliums in situ untersucht werden. Es zeigt sich hierbei, dass die Änderunge in den Au 4f Signalen reversibel sind und mit der Bildung eines Ga_2O_3 Filmes auf der Probenoberfläche wieder verschwinden. In Anlehnung an die mit den Pt/Pd/Rh-Ga Mischungen durchgeführten Experimente könnten Folgeexperimente die Untersuchung von Lösungen von Gold in flüssigem Gallium einschließen.

7. References

(1) van Santen, R. A., *Modern Heterogeneous Catalysis*; Viley VCH: 2017.

(2) Ertl, G. *Angewandte Chemie* **2009**, *121*, 6724–6730.

(3) *https://www.nobelprize.org/nobel_prizes/chemistry/laureates/1909/ostwald-bio.html (Accessed on 2018/05/17)*.

(4) Ostwald, W. *Physikalische Zeitschrift* **1902**, *3*, 313.

(5) Hagen, J., *Industrial Catalysis*; Wiley VCH Verlag GmbH: 2015.

(6) *Handbook of Heterogeneous Catalysis, 5 Volume Set*; Ertl, G., Ed.; Wiley-VCH: 1997.

(7) Mross, W. D. *Catalysis Reviews* **1983**, *25*, 591–637.

(8) Hutchings, G. J. *Catalysis Letters* **2001**, *75*, 1–12.

(9) Ponec, V. *Catalysis Reviews* **1975**, *11*, 41–70.

(10) Clarke, J. K. A. *Chemical Reviews* **1975**, *75*, 291–305.

(11) Senkan, S. *Angewandte Chemie International Edition* **2001**, *40*, 312–329.

(12) Hahndorf, I.; Buyevskaya, O.; Langpape, M.; Grubert, G.; Kolf, S.; Guillon, E.; Baerns, M. *Chemical Engineering Journal* **2002**, *89*, 119–125.

(13) Scheidtmann, J.; Weiß, P. A.; Maier, W. F. *Applied Catalysis A: General* **2001**, *222*, 79–89.

(14) *Modeling and Simulation of Heterogeneous Catalytic Reactions*; Deutschmann, O., Ed.; Wiley VCH Verlag GmbH: 2011.

(15) Maestri, M.; Cuoci, A. *Chemical Engineering Science* **2013**, *96*, 106–117.

(16) Matera, S.; Reuter, K. *Catalysis Letters* **2009**, *133*, 156–159.

(17) Sabbe, M. K.; Reyniers, M.-F.; Reuter, K. *Catalysis Science & Technology* **2012**, *2*, 2010.

(18) Greeley, J.; Mavrikakis, M. *Nature Materials* **2004**, *3*, 810–815.

(19) Nørskov, J. K.; Bligaard, T.; Rossmeisl, J.; Christensen, C. H. *Nature Chemistry* **2009**, *1*, 37–46.

(20) Föttinger, K.; van Bokhoven, J. A.; Nachtegaal, M.; Rupprechter, G. *The Journal of Physical Chemistry Letters* **2011**, *2*, 428–433.

(21) Salmeron, M.; Schlogl, R. *Surface Science Reports* **2008**, *63*, 169–199.

(22) Ogletree, D. F.; Bluhm, H.; Hebenstreit, E. D.; Salmeron, M. *Nuclear Instruments and Methods in Physics Research Section A: Accelerators, Spectrometers, Detectors and Associated Equipment* **2009**, *601*, 151–160.

(23) Starr, D. E.; Liu, Z.; Hävecker, M.; Knop-Gericke, A.; Bluhm, H. *Chemical Society Reviews* **2013**, *42*, 5833.

(24) Haghofer, A.; Föttinger, K.; Girgsdies, F.; Teschner, D.; Knop-Gericke, A.; Schlögl, R.; Rupprechter, G. *Journal of Catalysis* **2012**, *286*, 13–21.

(25) Rameshan, C.; Stadlmayr, W.; Penner, S.; Lorenz, H.; Mayr, L.; Hävecker, M.; Blume, R.; Rocha, T.; Teschner, D.; Knop-Gericke, A.; Schlögl, R.; Zemlyanov, D.; Memmel, N.; Klötzer, B. *Journal of Catalysis* **2012**, *290*, 126–137.

(26) Haghofer, A.; Föttinger, K.; Nachtegaal, M.; Armbrüster, M.; Rupprechter, G. *The Journal of Physical Chemistry C* **2012**, *116*, 21816–21827.

(27) Bordiga, S.; Groppo, E.; Agostini, G.; van Bokhoven, J. A.; Lamberti, C. *Chemical Reviews* **2013**, *113*, 1736–1850.

(28) Weckhuysen, B. M. *Chemical Communications* **2002**, 97–110.

(29) Breitkopf, C.; Papp, H.; Li, X.; Olindo, R.; Lercher, J. A.; Lloyd, R.; Wrabetz, S.; Jentoft, F. C.; Meinel, K.; Förster, S.; Schindler, K.-M.; Neddermeyer, H.; Widdra, W.; Hofmann, A.; Sauer, J. *Physical Chemistry Chemical Physics* **2007**, *9*, 3600–3618.

(30) Bäumer, M.; Libuda, J.; Neyman, K. M.; Rösch, N.; Rupprechter, G.; Freund, H.-J. *Physical Chemistry Chemical Physics* **2007**, *9*, 3541–3558.

(31) Oosterbeek, H. *Physical Chemistry Chemical Physics* **2007**, *9*, 3570–3576.

(32) Vang, R. T.; Lægsgaard, E.; Besenbacher, F. *Physical Chemistry Chemical Physics* **2007**, *9*, 3460–3469.

(33) Imbihl, R.; Scheibe, A.; Zeng, Y. F.; Günther, S.; Kraehnert, R.; Kondratenko, V. A.; Baerns, M.; Offermans, W. K.; Jansen, A. P. J.; van Santen, R. A. *Physical Chemistry Chemical Physics* **2007**, *9*, 3522–3540.

(34) Kampe, P.; Giebeler, L.; Samuelis, D.; Kunert, J.; Drochner, A.; Haaß, F.; Adams, A. H.; Ott, J.; Endres, S.; Schimanke, G.; Buhrmester, T.; Martin, M.; Fuess, H.; Vogel, H. *Physical Chemistry Chemical Physics* **2007**, *9*, 3577–3589.

(35) Reichelt, R.; Günther, S.; Rößler, M.; Wintterlin, J.; Kubias, B.; Jakobi, B.; Schlögl, R. *Physical Chemistry Chemical Physics* **2007**, *9*, 3590–3599.

(36) Neyman, K. M.; Lim, K. H.; Chen, Z.-X.; Moskaleva, L. V.; Bayer, A.; Reindl, A.; Borgmann, D.; Denecke, R.; Steinrück, H.-P.; Rösch, N. *Physical Chemistry Chemical Physics* **2007**, *9*, 3470–3482.

(37) Blume, R.; Hävecker, M.; Zafeiratos, S.; Teschner, D.; Vass, E.; Schnörch, P.; Knop-Gericke, A.; Schlögl, R.; Lizzit, S.; Dudin, P.; Barinov, A.; Kiskinova, M. *Physical Chemistry Chemical Physics* **2007**, *9*, 3648–3657.

(38) Haq, S.; Raval, R. *Physical Chemistry Chemical Physics* **2007**, *9*, 3641.

(39) Punckt, C.; Rotermund, H. H. *Physical Chemistry Chemical Physics* **2007**, *9*, 3635.

(40) Bowker, M. *Physical Chemistry Chemical Physics* **2007**, *9*, 3514.

(41) Bron, M.; Teschner, D.; Knop-Gericke, A.; Jentoft, F. C.; Kröhnert, J.; Hohmeyer, J.; Volckmar, C.; Steinhauer, B.; Schlögl, R.; Claus, P. *Physical Chemistry Chemical Physics* **2007**, *9*, 3559–3569.

(42) Zecchina, A.; Rivallan, M.; Berlier, G.; Lamberti, C.; Ricchiardi, G. *Physical Chemistry Chemical Physics* **2007**, *9*, 3483.

(43) Schüle, A.; Nieken, U.; Shekhah, O.; Ranke, W.; Schlögl, R.; Kolios, G. *Physical Chemistry Chemical Physics* **2007**, *9*, 3619–3634.

(44) Somorjai, G. A.; York, R. L.; Butcher, D.; Park, J. Y. *Physical Chemistry Chemical Physics* **2007**, *9*, 3500–3513.

(45) Bhasin, M. M.; McCain, J. H.; Vora, B. V.; Imai, T.; Pujadó, P. R. *Applied Catalysis A: General* **2001**, *221*, 397–419.

(46) Bricker, J. C. *Topics in Catalysis* **2012**, *55*, 1309–1314.

(47) Nawaz, Z. *Reviews in Chemical Engineering* **2015**, *31*, 413–436.

(48) Nawaz, Z. *International Journal of Chemical Reactor Engineering* **2016**, *14*, 491–515.

(49) Sattler, J. J. H. B.; Ruiz-Martinez, J.; Santillan-Jimenez, E.; Weckhuysen, B. M. *Chemical Reviews* **2014**, *114*, 10613–10653.

(50) Wang, S.; Zhu, Z. H. *Energy & Fuels* **2004**, *18*, 1126–1139.

(51) Mamedov, E. A.; Corberán, V. C. *Applied Catalysis A: General* **1995**, *127*, 1–40.

(52) Cavani, F.; Ballarini, N.; Cericola, A. *Catalysis Today* **2007**, *127*, 113–131.

(53) Grabowski, R. *Catalysis Reviews* **2006**, *48*, 199–268.

(54) Sattler, J. J. H. B.; Gonzalez-Jimenez, I. D.; Luo, L.; Stears, B. A.; Malek, A.; Barton, D. G.; Kilos, B. A.; Kaminsky, M. P.; Verhoeven, T. W. G. M.; Koers, E. J.; Baldus, M.; Weckhuysen, B. M. *Angewandte Chemie International Edition* **2014**, *53*, 9251–9256.

(55) Redekop, E. A.; Galvita, V. V.; Poelman, H.; Bliznuk, V.; Detavernier, C.; Marin, G. B. *ACS Catalysis* **2014**, *4*, 1812–1824.

(56) Siddiqi, G.; Sun, P.; Galvita, V.; Bell, A. T. *Journal of Catalysis* **2010**, *274*, 200–206.

(57) Jablonski, E. L.; Castro, A. A.; Scelza, O. A.; de Miguel, S. R. *Applied Catalysis A: General* **1999**, *183*, 189–198.

(58) Sun, P.; Siddiqi, G.; Chi, M.; Bell, A. T. *Journal of Catalysis* **2010**, *274*, 192–199.

(59) Iwasa, N.; Mayanagi, T.; Ogawa, N.; Sakata, K.; Takezawa, N. *Catalysis Letters* **1998**, *54*, 119–123.

(60) Iwasa, N. *Topics in Catalysis* **2003**, *22*, 215–224.

(61) Lorenz, H.; Penner, S.; Jochum, W.; Rameshan, C.; Klötzer, B. *Applied Catalysis A: General* **2009**, *358*, 203–210.

(62) Penner, S.; Lorenz, H.; Jochum, W.; Stöger-Pollach, M.; Wang, D.; Rameshan, C.; Klötzer, B. *Applied Catalysis A: General* **2009**, *358*, 193–202.

(63) Osswald, J.; Kovnir, K.; Armbrüster, M.; Giedigkeit, R.; Jentoft, R.; Wild, U.; Grin, Y.; Schlögl, R. *Journal of Catalysis* **2008**, *258*, 219–227.

(64) Osswald, J.; Giedigkeit, R.; Jentoft, R.; Armbruster, M.; Girgsdies, F.; Kovnir, K.; Ressler, T.; Grin, Y.; Schlogl, R. *Journal of Catalysis* **2008**, *258*, 210–218.

(65) Kovnir, K.; Armbrüster, M.; Teschner, D.; Venkov, T. V.; Szentmiklósi, L.; Jentoft, F. C.; Knop-Gericke, A.; Grin, Y.; Schlögl, R. *Surface Science* **2009**, *603*, 1784–1792.

(66) Kovnir, K.; Osswald, J.; Armbrüster, M.; Teschner, D.; Weinberg, G.; Wild, U.; Knop-Gericke, A.; Ressler, T.; Grin, Y.; Schlögl, R. *Journal of Catalysis* **2009**, *264*, 93–103.

(67) Armbrüster, M.; Kovnir, K.; Behrens, M.; Teschner, D.; Grin, Y.; Schlögl, R. *Journal of the American Chemical Society* **2010**, *132*, 14745–14747.

(68) Ota, A.; Armbrüster, M.; Behrens, M.; Rosenthal, D.; Friedrich, M.; Kasatkin, I.; Girgsdies, F.; Zhang, W.; Wagner, R.; Schlögl, R. *The Journal of Physical Chemistry C* **2010**, *115*, 1368–1374.

(69) Li, L.; Zhang, B.; Kunkes, E.; Föttinger, K.; Armbrüster, M.; Su, D. S.; Wei, W.; Schlögl, R.; Behrens, M. *ChemCatChem* **2012**, *4*, 1764–1775.

(70) Wowsnick, G.; Teschner, D.; Kasatkin, I.; Girgsdies, F.; Armbrüster, M.; Zhang, A.; Grin, Y.; Schlögl, R.; Behrens, M. *Journal of Catalysis* **2014**, *309*, 209–220.

(71) Wowsnick, G.; Teschner, D.; Armbrüster, M.; Kasatkin, I.; Girgsdies, F.; Grin, Y.; Schlögl, R.; Behrens, M. *Journal of Catalysis* **2014**, *309*, 221–230.

(72) Armbrüster, M.; Schlögl, R.; Grin, Y. *Science and Technology of Advanced Materials* **2014**, *15*, 034803.

(73) Polak, M.; Rubinovich, L. *Surface Science Reports* **2000**, *38*, 127–194.

(74) Anres, P.; Gaune-Escard, M.; Bros, J. *Journal of Alloys and Compounds* **1996**, *234*, 264–274.

(75) Li, M.; Li, C.; Wang, F.; Zhang, W. *Intermetallics* **2006**, *14*, 826–831.

(76) Gröbner, J.; Wenzel, R.; Fischer, G. G.; Schmid-Fetzer, R. *Journal of Phase Equilibria* **1999**, *20*, 615–625.

(77) Anres, P.; Gaune-Escard, M.; Bros, J. P. *Journal of Alloys and Compounds* **1998**, *265*, 201–208.

(78) Allam, D. E.; Gaune-Escard, M.; Bros, J.-P.; Hayer, E. *Metallurgical Transactions B* **1992**, *23*, 39–44.

(79) Vitos, L.; Ruban, A. V.; Skriver, H. L.; Kollár, J. *Surface Science* **1998**, *411*, 186–202.

(80) Tyson, W. R.; Miller, W. A. *Surface Science* **1977**, *62*, 267–276.

(81) Seah, M. *Journal of Catalysis* **1979**, *57*, 450–457.

(82) Williams, F. L.; Nason, D. *Surface Science* **1974**, *45*, 377–408.

(83) Hertz, H. *Annalen der Physik und Chemie* **1887**, *267*, 983–1000.

(84) Einstein, A. *Annalen der Physik* **1905**, *322*, 132–148.

(85) Siegbahn, K. *Reviews of Modern Physics* **1982**, *54*, 709–728.

(86) *http://www.nobelprize.org/nobel_prizes/physics/laureates/1981/siegbahn-cv.html (Accessed on 2018/04/16)*.

(87) Hüfner, S., *Photoelectron Spectroscopy*; Springer: 2003.

(88) Axnanda, S.; Scheele, M.; Crumlin, E.; Mao, B.; Chang, R.; Rani, S.; Faiz, M.; Wang, S.; Alivisatos, A. P.; Liu, Z. *Nano Letters* **2013**, *13*, 6176–6182.

(89) Werner, W. S. M. *Surface and Interface Analysis* **2001**, *31*, 141–176.

(90) Deuring, A.; Floeder, K.; Fromme, D.; Raith, W.; Schwab, A.; Sinapius, G.; Zitzewitz, P. W.; Krug, J. *Journal of Physics B: Atomic and Molecular Physics* **1983**, *16*, 1633–1656.

(91) Floeder, K.; Fromme, D.; Raith, W.; Schwab, A.; Sinapius, G. *Journal of Physics B: Atomic and Molecular Physics* **1985**, *18*, 3347–3359.

(92) Garcia, G.; Aragón, C.; Campos, J. *Physical Review A* **1990**, *42*, 4400–4402.

(93) Jain, A.; Baluja, K. L. *Physical Review A* **1992**, *45*, 202–218.

(94) Garcia, G.; Manero, F. *Physical Review A* **1996**, *53*, 250–254.

(95) Tanuma, S.; Powell, C. J.; Penn, D. R. *Surface and Interface Analysis* **1991**, *17*, 927–939.

(96) Seah, M. P. *Surface and Interface Analysis* **1980**, *2*, 222–239.

(97) Vulli, M. *Surface and Interface Analysis* **1981**, *3*, 67–71.

(98) Scofield, J. *Journal of Electron Spectroscopy and Related Phenomena* **1976**, *8*, 129–137.

(99) Yeh, J.; Lindau, I. *Atomic Data and Nuclear Data Tables* **1985**, *32*, 1–155.

(100) Ruffieux, P.; Schwaller, P.; Gröning, O.; Schlapbach, L.; Gröning, P.; Herd, Q. C.; Funnemann, D.; Westermann, J. *Review of Scientific Instruments* **2000**, *71*, 3634.

(101) Paynter, R. W. *Surface and Interface Analysis* **1981**, *3*, 186–187.

(102) Jeurgens, L.; Sloof, W.; Tichelaar, F.; Mittemeijer, E. *Surface Science* **2002**, *506*, 313–332.

(103) Scrocco, M. *physica status solidi (b)* **1984**, *125*, 713–720.

(104) Leiro, J.; Heinonen, M. *Surface Science* **1996**, *346*, 73–78.

(105) Simonsen, A. C.; Yubero, F.; Tougaard, S. *Physical Review B* **1997**, *56*, 1612–1619.

(106) Yubero, F.; Kover, L.; Drube, W.; Eickhoff, T.; Tougaard, S. *Surface Science* **2005**, *592*, 1–7.

(107) Yubero, F.; Tougaard, S. *Physical Review B* **2005**, *71*, 045414.

(108) Niedermaier, I.; Kolbeck, C.; Steinrück, H.-P.; Maier, F. *Review of Scientific Instruments* **2016**, *87*, 045105.

(109) Pantförder, J.; Pöllmann, S.; Zhu, J. F.; Borgmann, D.; Denecke, R.; Steinrück, H.-P. *Review of Scientific Instruments* **2005**, *76*, 014102.

(110) Pantförder, J. Photoelektronenspektroskopie im Pressure Gap - Aufbau einer neuen Apparatur für Messungen im Druckbereich von 10E-10 bis 1 mbar., Disseration thesis.

(111) Grabau, M.; Calderón, S. K.; Rietzler, F.; Niedermaier, I.; Taccardi, N.; Wasserscheid, P.; Maier, F.; Steinrück, H.-P.; Papp, C. *Surface Science* **2016**, *651*, 16–21.

(112) Grabau, M.; Erhard, J.; Taccardi, N.; Calderon, S. K.; Wasserscheid, P.; Görling, A.; Steinrück, H.-P.; Papp, C. *Chemistry - A European Journal* **2017**, *23*, 17701–17706.

(113) Grabau, M.; Steinrück, H.-P.; Papp, C. *Surface Science* **2018**, *677*, 254–257.

(114) Taccardi, N.; Grabau, M.; Debuschewitz, J.; Distaso, M.; Brandl, M.; Hock, R.; Maier, F.; Papp, C.; Erhard, J.; Neiss, C.; Peukert, W.; Görling, A.; Steinrück, H.-P.; Wasserscheid, P. *Nature Chemistry* **2017**, *9*, 862–867.

(115) Fleisch, T. H.; Hicks, R. F.; Bell, A. T. *Journal of Catalysis* **1984**, *87*, 398–413.

(116) Yan, Y. L.; Helfand, M. A.; Clayton, C. R. *Applied Surface Science* **1989**, *37*, 395–405.

(117) Bond, G. C., *Metal-Catalysed Reactions of Hydrocarbons*; Springer-Verlag GmbH: 2005.

(118) Hondros, E. D.; Seah, M. P. *Metallurgical Transactions A* **1977**, *8*, 1363–1371.

(119) Overbury, S. H.; Bertrand, P. A.; Somorjai, G. A. *Chemical Reviews* **1975**, *75*, 547–560.

(120) Speiser, R.; Johnston, H. L. *Journal of the American Chemical Society* **1953**, *75*, 1469–1470.

(121) Zavitsanos, P. D. *The Journal of Physical Chemistry* **1964**, *68*, 2899–2901.

(122) Surdu-Bob, C.; Saied, S.; Sullivan, J. *Applied Surface Science* **2001**, *183*, 126–136.

(123) Schön, G. *Journal of Electron Spectroscopy and Related Phenomena* **1973**, *2*, 75–86.

(124) Carli, R.; Bianchi, C. *Applied Surface Science* **1994**, *74*, 99–102.

(125) Chabala, J. M. *Physical Review B* **1992**, *46*, 11346–11357.

(126) Atkinson, A. *Reviews of Modern Physics* **1985**, *57*, 437–470.

(127) Cabrera, N.; Mott, N. F. In *World Scientific Series in 20th Century Physics*; WORLD SCIENTIFIC: 1995, pp 185–207.

(128) Regan, M. J.; Tostmann, H.; Pershan, P. S.; Magnussen, O. M.; DiMasi, E.; Ocko, B. M.; Deutsch, M. *Physical Review B* **1997**, *55*, 10786–10790.

(129) Wagner, C. D.; Davis, L. E.; Zeller, M. V.; Taylor, J. A.; Raymond, R. H.; Gale, L. H. *Surface and Interface Analysis* **1981**, *3*, 211–225.

(130) Miller, D. J.; Öberg, H.; Kaya, S.; Casalongue, H. S.; Friebel, D.; Anniyev, T.; Ogasawara, H.; Bluhm, H.; Pettersson, L. G. M.; Nilsson, A. *Physical Review Letters* **2011**, *107*, 195502.

(131) Butcher, D. R.; Grass, M. E.; Zeng, Z.; Aksoy, F.; Bluhm, H.; Li, W.-X.; Mun, B. S.; Somorjai, G. A.; Liu, Z. *Journal of the American Chemical Society* **2011**, *133*, 20319–20325.

(132) Peuckert, M.; Bonzel, H. *Surface Science* **1984**, *145*, 239–259.

(133) Parkinson, C.; Walker, M.; McConville, C. *Surface Science* **2003**, *545*, 19–33.

(134) Jung, M.-C.; Kim, H.-D.; Han, M.; Jo, W.; Kim, D. C. *Japanese Journal of Applied Physics* **1999**, *38*, 4872–4875.

(135) Fleisch, T. H.; Mains, G. J. *The Journal of Physical Chemistry* **1986**, *90*, 5317–5320.

(136) Bancroft, G. M.; Adams, I.; Coatsworth, L. L.; Bennewitz, C. D.; Brown, J. D.; Westwood, W. D. *Analytical Chemistry* **1975**, *47*, 586–588.

(137) Ellinger, C.; Stierle, A.; Robinson, I. K.; Nefedov, A.; Dosch, H. *Journal of Physics: Condensed Matter* **2008**, *20*, 184013.

(138) Neitzel, A.; Figueroba, A.; Lykhach, Y.; Skála, T.; Vorokhta, M.; Tsud, N.; Mehl, S.; Ševčíková, K.; Prince, K. C.; Neyman, K. M.; Matolín, V.; Libuda, J. *The Journal of Physical Chemistry C* **2016**, *120*, 9852–9862.

(139) Venezia, A. *Journal of Catalysis* **2003**, *215*, 317–325.

(140) Xu, J.; White, T.; Li, P.; He, C.; Yu, J.; Yuan, W.; Han, Y.-F. *Journal of the American Chemical Society* **2010**, *132*, 10398–10406.

(141) Chen, M.; Kumar, D.; Yi, C.-W.; Goodman, D. W. *Science* **2005**, *310*, 291–293.

(142) Haruta, M. *The Chemical Record* **2003**, *3*, 75–87.

(143) Hashmi, A. S. K.; Hutchings, G. J. *Angewandte Chemie International Edition* **2006**, *45*, 7896–7936.

(144) Meyer, R.; Lemire, C.; Shaikhutdinov, S. K.; Freund, H. J. *Gold Bulletin* **2004**, *37*, 72–124.

(145) Min, B. K.; Friend, C. M. *Chemical Reviews* **2007**, *107*, 2709–2724.

(146) Yang, X.-F.; Wang, A.; Qiao, B.; Li, J.; Liu, J.; Zhang, T. *Accounts of Chemical Research* **2013**, *46*, 1740–1748.

(147) Haruta, M. *Catalysis Today* **1997**, *36*, 153–166.

(148) Haruta, M. *CATTECH* **2002**, *6*, 102–115.

(149) Lucci, F. R.; Darby, M. T.; Mattera, M. F. G.; Ivimey, C. J.; Therrien, A. J.; Michaelides, A.; Stamatakis, M.; Sykes, E. C. H. *The Journal of Physical Chemistry Letters* **2016**, *7*, 480–485.

(150) Lucci, F. R.; Liu, J.; Marcinkowski, M. D.; Yang, M.; Allard, L. F.; Flytzani-Stephanopoulos, M.; Sykes, E. C. H. *Nature Communications* **2015**, *6*, DOI: 10.1038/ncomms9550.

(151) Liu, J.; Lucci, F. R.; Yang, M.; Lee, S.; Marcinkowski, M. D.; Therrien, A. J.; Williams, C. T.; Sykes, E. C. H.; Flytzani-Stephanopoulos, M. *Journal of the American Chemical Society* **2016**, *138*, 6396–6399.

(152) Dürrwächter, M.; Indlekofer, G.; Boyen, H.-G.; Oelhafen, P.; Quitmann, D. *Journal of Non-Crystalline Solids* **1993**, *156-158*, 241–245.

(153) Elliott, R. P.; Shunk, F. A. *Bulletin of Alloy Phase Diagrams* **1981**, *2*, 356–358.

(154) Liu, J.; Guo, C.; Li, C.; Du, Z. *Journal of Alloys and Compounds* **2010**, *508*, 62–70.

8. Acknowledgments

First of all, I want to dedicate this thesis to Hannah, Nina and my family. I want to express all of them my gratitude for love, patience and constant support.

I also want to thank Prof. Dr. Steinrück for the opportunity to work on this thesis in an outstandingly free and supporting environment and for many fruitful discussions. Furthermore, I want to thank Dr. Christian Papp for supervision, for numerous discussions and uncounted, precious advices. It has always been a pleasure to argue with you.

I also owe gratitude to all colleagues and friends at the chair, in particular to Flo and Flo, Michi and Michi, Sandra, Bernd, and HP for their help, support, many discussions and a lovely working atmosphere.

9. The author's contributions to P1 – P4

The author's contributions to the published articles P1 to P4 are listed in the following.

P1 Measurement, analysis and interpretation of XPS data, authorship.

P2 Measurement, analysis and interpretation of XPS data, authorship.

P3 Measurement, analysis and interpretation of all shown data, authorship.

P4 Measurement, analysis and interpretation of all shown data, authorship.

A. Appendix A

A.1. P1

Gallium-rich Pd-Ga phases as supported liquid metal catalysts

N. Taccardi†, M. Grabau†, J. Debuschewitz, M. Distaso, M. Brandl, R. Hock, F. Maier, C. Papp, J. Erhard, C. Neiss, W. Peukert, A. Görling, H.-P. Steinrück, P. Wasserscheid

Nature Chemistry, **2017**, 9, 862–867.
https://doi.org/10.1038/nchem.2822

† shared first-authorship

A.2. P2

Spectroscopic Observation and Molecular Dynamics Simulation of Ga Surface Segregation in Liquid Pd-Ga Alloys

M. Grabau[†], J. Erhard[†], N. Taccardi, S. Krick Calderón, P. Wasserscheid, A. Görling, H.-P. Steinrück, C. Papp

Chemistry A European Journal, **2017**, 23, 17701–17706.
https://doi.org/10.1002/chem.201703627

[†] shared first-authorship

A.3. P3

Surface enrichment of Pt in Ga_2O_3 films grown on liquid Pt/Ga alloys

M. Grabau, S. Krick Calderón, F. Rietzler, I. Niedermaier, N. Taccardi, P. Wasserscheid, F. Maier, H.-P. Steinrück, C. Papp

Surface Science, **2016**, 651, 16–21.
https://doi.org/10.1016/j.susc.2016.03.009

A.4. P4

Physical vapor deposition of Ga on polycrystalline Au surfaces studied using X-ray photoelectron spectroscopy

M. Grabau, H.-P. Steinrück, C. Papp

Surface Science, **2018**, 677, 254–257.
https://doi.org/10.1016/j.susc.2018.07.011

B. Appendix B

B.1. Ga evaporator

Figure B.1.: Ga evaporator used for the deposition of Ga onto Au surfaces. Used is an Al_2O_3 crucible of 8 mm inner- and 10 mm outer diameter, which is fitted into a solenoid from tungsten wire of 0.5 mm diameter. Crucible temperature was measured using a type K thermocouple pressed to the outer bottom of the crucible. Typically powers to achieve crucible temperatures above 800 K exceeded $10 \cdot 12\,\mathrm{V\,A}$.

B.2. Drawings aperature a_1